Reactive oxygen species responsive dextran-thioketal conjugate nanocarriers for the delivery of hydrophilic payloads

Sourav Nayak [1,2], Nuran Caz [3], Elien Derveaux [1,2], Sander Smeets [1,2], Tom Cardeynaels [1,2], Esther Wolfs [3], Peter Adriaensens [1,2], Wouter Maes [1,2] and Anitha Ethirajan* [1,2]

[1] Hasselt University, Institute for Materials Research (imo-imomec), Martelarenlaan 42, B-3500 Hasselt, Belgium

[2] imec, imo-imomec, Wetenschapspark 1, B-3590 Diepenbeek, Belgium

[3] Hasselt University, BIOMED, Laboratory for Functional Imaging & Research on Stem Cells (FIERCE Lab), Agoralaan gebouw C, B-3590 Diepenbeek, Belgium

*Corresponding author: Prof. Anitha Ethirajan; E-mail: anitha.ethirajan@uhasselt.be

Abstract:

Dextran-thioketal conjugate (DTKC) nanocarrier responsive to endogenous as well as exogenous stimuli is developed for delivering hydrophilic payloads. First, water-soluble reactive oxygen species (ROS)-responsive DTKCs are synthesized and responsiveness to various ROS stimuli is studied. Next, different DTKC nanocarriers (NCs) loaded with the respective hydrophilic molecules -fluorescent dye (rhodamine B, RhoB), photosensitizer, PS (rose bengal, RB), and chemotherapeutic drug (doxorubicin hydrochloride, Dox)- are synthesized using inverse miniemulsion interfacial polymerization. All NCs exhibit nanocapsule morphology, and cargo dependent hydrodynamic diameters (166–194 nm) in water, an encapsulation efficiency between 79-91%, and a drug loading content of about 11%. RhoB-NCs and Dox-NCs exhibit time-dependent release upon exposure to different H_2O_2 concentrations and an enhanced release in conditioned medium collected from oral squamous cell carcinoma (OSCC) cells. Further, as a proof-of-concept, light-responsive payload release from PS loaded NCs via a cascade reaction is confirmed. The in vitro studies show that RhoB-NCs and RB-NCs are biocompatible while the Dox-NCs exhibit cytotoxic effects. Such dextran-based ROS-responsive NCs sensitive to endogenous (ROS rich environment) as well as exogenous (light in combination with a PS) stimuli are highly interesting to realize combination therapies, for instance combining a chemotherapeutic drug and a photosensitizer for application in photochemotherapy.

Keywords: Dextran-thioketal conjugate, nanocapsules, ROS responsive release, light responsive release, drug delivery, cancer cells

1. Introduction

Stimuli-responsive nanocarriers (NCs) that undergo physicochemical or morphological transition upon exposure to a desired stimulus of action exhibit immense potential for the delivery of cancer therapeutics (Fatima et al., 2024; Shi et al., 2024; Tang et al., 2024). NCs with responsiveness to various stimuli, whether external (such as magnetic, light, ultrasound, and temperature) or internal (including pH, redox, hypoxia, enzyme, etc.), have been synthesized and extensively investigated for *in vitro* and *in vivo* studies involving cancer cells (Liu et al., 2024; Mi, 2020; Mura, Nicolas, & Couvreur, 2013) in the context of chemotherapy, photodynamic therapy, imaging, immunotherapy, and gene therapy. (Zhang et al., 2023; Kaushik et al., 2022; Chang et al., 2021; Torchilin, 2014). Recently, reactive oxygen species (ROS) as a stimulus has received increased attention for designing different drug delivery systems (DDSs), particularly for drug resistant and ROS-elevated tumor cells (Yang et al., 2022). Tumor cells are associated with overproduction of ROS species as compared to healthy cells, caused by environmental and many internal factors including mitochondrial dysfunction, increased growth signals, decreased antioxidants, and others (Yang et al., 2018). This enhanced level of ROS opens up a therapeutic window for the delivery of drugs to cancer cells via the enhanced permeability and retention (EPR) effect. A variety of polymers, including cationic poly(amino thioketal) (PATK) (Shim, & Xia, 2013), poly(ester-thioacetal) (Xu et al., 2018), phenylborate ester (PBAE) polymers (Liu et al., 2020), and poly(tetraphenylethylene-aminoacrylate-oligoethylenimine)-mPEG grafted copolymers (P(TPECM-AA-OEI)-g-mPEG) (Yuan, Zhang, & Liu, 2015) were synthesized using ROS-responsive thioketal, thioether, arylboronate ester, aminoacrylate chemical groups, respectively. Upon exposure to an oxidative stimulus, the chemical bond breaks at the responsive part of the polymer and exhibits a transition from a hydrophobic to a hydrophilic nature, resulting in loosening/swelling of the NCs and subsequently causing drug release (Gao, & Xiong, 2021). Mostly, these (co)polymeric NCs are formulated as self-assembled micelles through hydrophobic or electrostatic interactions, facilitating the encapsulation of hydrophobic drugs (Tyrrell, Shen, & Radosz, 2010).

Although synthetic polymers with controlled composition and molecular weight have been used for designing DDSs, biopolymers (e.g., dextran, hyaluronic acid, chitosan, alginate, etc.) have an edge over the former as they offer interesting intrinsic characteristics such as biocompatibility,

inherent biodegradability, low immunogenicity, and useful functional groups for chemical conjugation (Arora et al., 2021; Seidi, Jenjob, Phakkeeree, & Crespy, 2018). Particularly, dextran is extensively used for the delivery of tumor chemotherapeutic drugs because of its hydrophilicity, good solubility in different solvents (e.g. water, DMSO, formamide, ethylene glycol, and glycerol), prolonged blood circulation ability, biodegradability (Hu, Lu, & Luo, 2021), and biocompatibility (Huang, & Huang, 2018). Pramod et al. synthesized dextran vesicular nanoscaffolds by coupling hydrophobic units to dextran for the co-delivery of water-soluble molecules and the polyaromatic anticancer drug camptothecin (Pramod et al., 2012). Furthermore, acid-sensitive ROS-triggered dextran-based DDSs were developed for chemo-photodynamic cancer therapy, where the chemotherapeutic doxorubicin was chemically conjugated to the dextran backbone using a ROS-cleavable thioketal linker, while the porphyrin photosensitizer (Zn-TPP) was encapsulated via metal coordination (Bao, Yin, Liu, & Chen, 2020). Alkanawati et al. developed pH-sensitive NCs using bio-orthogonal chemistry by crosslinking aldehyde/ketone-functionalized dextran with poly(styrene-co-methacryloyl hydrazide) for the delivery of sensitive biomacromolecular therapeutic agents such as proteins, DNA, or RNA (Alkanawati et al., 2020). Although these reports show the potential of dextran-based DDSs, using ROS-responsive dextran-based DDS for hydrophilic drugs is still in its infancy. Moreover, the dextran based NCs are mostly formulated as self-assembled micelles where hydrophilic dextran is modified by a hydrophobic linker and/or prodrug conjugates and thus can only load hydrophobic molecules into the core of the micelles or hydrophilic drugs via chemical conjugation (Fazal et al., 2023). Despite the ability of these NCs to release payloads both *in vitro* and *in vivo*, they often encounter challenges such as disassembly in cellular medium, premature drug release at non-target sites, cytotoxicity, and/or the requirement of toxic solvents and catalysts (Perumal, Atchudan, & Lee, 2022; Tyrrell, Shen, & Radosz, 2010).

In this study, we report a water-soluble dextran-thioketal conjugate (DTKC) which is obtained by crosslinking a thioketal linker at the glucose units of different chains of dextran, and the conjugate is tested against various ROS species found in cancer cells. The hydrophobic thioketal moiety is chosen due to its reactivity to various ROS species, biodegradability, and amenability to incorporation in polymers (Rinaldi et al., 2022). We hypothesize that thioketal conjugated dextran with high substitution retaining water solubility can be used to formulate ROS responsive dextran based NCs that are sensitive to various ROS species present in the biological

environment and also can be triggered by light in the presence of a photosensitizer to release hydrophilic payloads. The NCs are expected to deliver hydrophilic therapeutics employing endogenous (ROS rich environment) and exogenous (light) stimuli. Using the conjugate with the highest degree of substitution, dextran-thioketal nanocarriers (DTKC-NCs) with urethane linkages are synthesized to encapsulate various hydrophilic payloads through the inverse miniemulsion interfacial polymerization technique (Tiwari et. al., 2021; Seneca et al., 2020; Pramanik et al., 2019; Iyisan, & Landfester, 2019; Pramanik et al., 2018). Three model payloads – rhodamine B (RhoB), rose bengal (RB), and doxorubicin (Dox) – are selected for their application as a fluorescent dye for imaging, a photosensitizer (PS) for photodynamic therapy, and a chemotherapeutic drug, respectively, and their release upon ROS exposure is studied (Fig. 1).

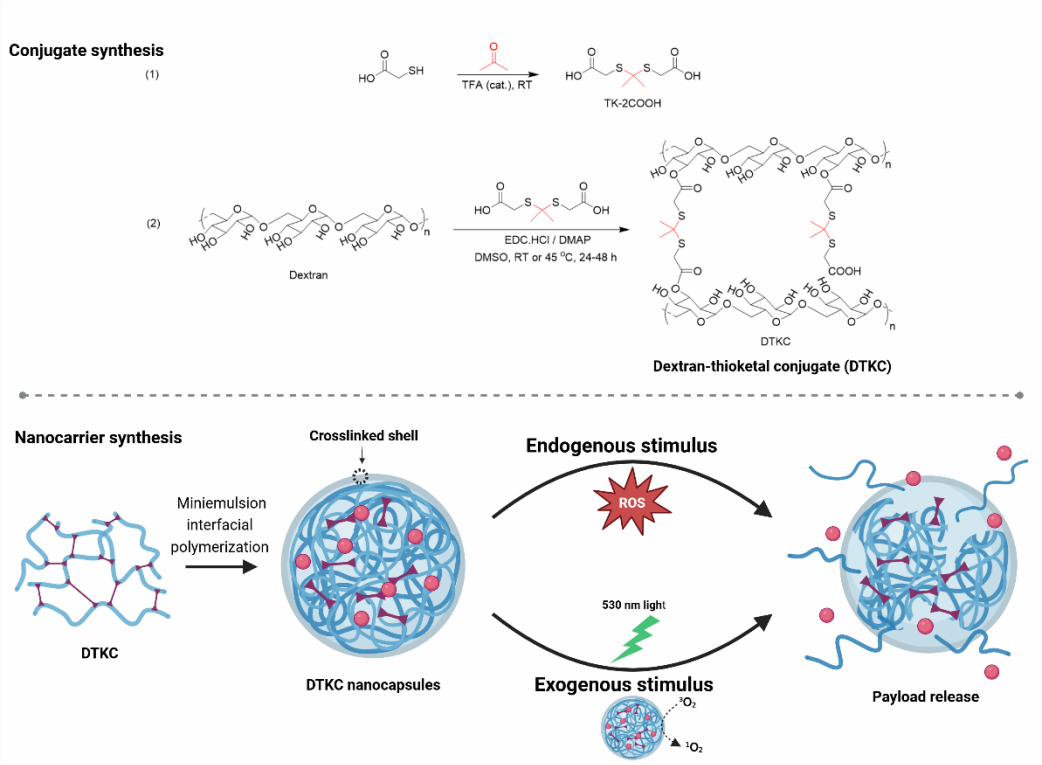

Fig. 1: Illustration of the thioketal linker (1) and the dextran-thioketal conjugate (2) synthesis. Next, the nanocarrier synthesis by miniemulsion interfacial crosslinking using TDI and the payload release from the nanocarriers upon exposure to an endogenous (elevated ROS in the biological environment) or an exogenous stimulus (light) via a cascade reaction of $^1O_2$ production and conjugate degradation are illustrated.

Interestingly here, the encapsulated PS can generate singlet oxygen upon irradiation with light of a suitable wavelength to cleave the thioketal linkers via a cascade reaction. Previously, light was

used to cleave a drug-conjugated TK linker in combination with up-conversion nanoparticles and a PS (Yue et al., 2016), whereas in our system, no drug conjugation is required but the drugs are encapsulated/protected by the degradable polymeric shell, offering flexibility in incorporating different active ingredients while maintaining their native structure and activity. The synthesized NCs are further studied for their biocompatibility and cellular uptake using an oral squamous cell carcinoma (OSCC) cell line. The latter is characterized by elevated levels of ROS (Kesarwala, Krishna, & Mitchell, 2016), thereby presenting an interesting target for the designed ROS-responsive NCs.

2. Materials and methods

2.1. Materials

Dextran (MW *ca.* = 40000, $(C_6H_{10}O_5)_n$; Thermo Scientific) was dried at 100 ºC in a vacuum oven overnight before use. *N*-(3-Dimethylaminopropyl)-*N*′-ethylcarbodiimide hydrochloride (EDC.HCl; Alfa Aesar, 98+%), 4-dimethylaminopyridine (DMAP; Thermo Scientific, 99%, pilled), and anhydrous dimethyl sulfoxide (Thermo Scientific, 99%) were used as received. Thioglycolic acid (TCI Europe, >95%), trifluoroacetic acid (TFA; Honeywell), acetone (Fischer Chemical, analytical grade, 99.9%), *n*-hexane (VWR chemicals, 98%), cyclohexane (Honeywell), methanol (VWR chemicals, ≥99.8%), sodium chloride (NaCl; VWR Chemical, 99.5%), toluene-2,4-diisocyanate (TDI; TCI Europe, >98%), rose bengal (RB; Thermo Scientific, 85%), rhodamine B (RhoB; Acros Organics, ≥98%), doxorubicin hydrochloride (DOX.HCl; Merck), 5,5-dithio-bis-(2-nitrobenzoic acid) (DTNB; Acros Organics, 99%), 1,3-diphenylisobenzofuran (DPBF; Sigma-Aldrich, 97%), and sodium dodecyl sulfate (SDS; Acros Organics, 99%) were used as obtained from the supplier. Deuterium oxide (D_2O; Thermo Scientific, 100.0% atom D), methyl sulfoxide-d_6 (DMSO-d_6; Thermo Scientific, 99.9 atom% D), and acetone-d_6 (Deutero GmbH, 99.8% atom D) were used as NMR solvents. Spectrum™ Spectra/Por™ 3 RC dialysis membrane tubing (MWCO 3500) was used for dialysis. The polymeric surfactant Hypermer B246 was obtained from Croda Europe Ltd (UK). Deionized water (DI) from a Sartorius Stedim Biotech machine was used for all experiments unless mentioned otherwise. BupH™ modified Dulbecco's phosphate buffered saline (PBS) packs were used (0.008 M sodium phosphate, 0.002 M potassium phosphate, 0.14 M sodium chloride, 0.0027 M potassium chloride) to make buffer

solutions of pH =7.4 in a final volume of 500 mL. The pH of the buffer solution was adjusted with 1 M NaOH or HCl solution to obtain the desired pH for the different experiments.

2.2. Synthesis of the thioketal (TK–2COOH) linker

The synthesis of 2,2'-(propane-2,2-diyl-bis(sulfanediyl))diacetic acid (TK–2COOH) was carried out according to a modified procedure from literature (Pan et al., 2020). Briefly, an oven-dried round bottom flask was charged with thioglycolic acid (15.7 g, 170.5 mmol) and acetone (4.5 g, 77.5 mmol) while stirring at room temperature (RT). A catalytic amount of TFA (~30 µL) was added to the reaction mixture and the flask was flushed with N_2. The reaction was allowed to stir overnight and then cooled in ice water to complete the crystallization of the white product. The precipitate was filtered off, washed with *n*-hexane and cold water several times, and vacuum dried (15.5 g; 89% yield). The linker molecule was characterized by ^{1}H and ^{13}C NMR spectroscopy (supplementary material, S1).

^{1}H NMR (400 MHz, DMSO-d_6, δ): 1.53 (s, 6H; C$\underline{H}_3$), 3.35 (s, 4H; C$\underline{H}_2$)

2.3. Synthesis of the dextran-thioketal conjugates

The conjugates were prepared by an esterification reaction between the carboxylic acid groups of the TK linker and the hydroxy groups of dextran (Fig. 1(2)). First, different amounts of TK−2COOH (0.5×, 1×, and 1.3× the number of equiv. of the anhydrous glucose units (AGU) of dextran) were stirred with EDC.HCl and DMAP, maintaining the molar ratio of TK-2COOH, EDC.HCl, and DMAP at 1:3:0.3, in anhydrous DMSO (15 mL) at RT and under an inert atmosphere for 2 h to preactivate the −COOH groups of the thioketal. Next, 0.81 g dextran (5 mmol, MW = 162 g/mol of the AGU unit) was dissolved in 10 mL anhydrous DMSO by heating at 45 ºC until complete dissolution. Then, the previously activated thioketal was added to the dextran solution drop wise and the reaction mixture was stirred at RT or 45 ºC under an inert atmosphere for 24‑48 h (see Table S1). After that, the reaction mixture was cooled to RT and the product was precipitated by adding the reaction mixture dropwise to an excess of cold acetone (300 mL). The precipitate was filtered off and washed with cold methanol (300 mL). Then, the precipitate was redissolved in DMSO and precipitated again according to the same procedure. After 3 consecutive purification steps, the product was dissolved in water and transferred into a dialysis bag (MWCO 3.5 kDa). Dialysis was carried out for 5 days against DI water, changing the

water twice a day. Finally, the dialyzed solution was lyophilized for 24 h, which resulted in a light brown product (yield between 51-63 %), stored in the fridge (4 ºC). The product was characterized by ^{1}H NMR, ^{13}C NMR, and ATR-FTIR spectroscopy.

The degree of substitution (DS_{TK}; see Table S1 and Fig. S2.1–2.5) was estimated by ^{1}H NMR according to the formula

$$DS_{TK} =$$

where the C1 anomeric protons from the glucose units of dextran appear at 4.95 ppm and the 6 methyl protons from the thioketal at 1.61 ppm in D_2O (Guo et al., 2024). Due to the presence of small overlapping peaks around 4.95 ppm in native dextran (see Fig. S2.1), the whole region between 4.8-5.4 ppm was included in the integration for the C1 anomeric protons.

2.4. Solubility test of the DTKCs

To check the solubility of the conjugates in water, known excess amounts of the conjugates were taken in 3 mL of DI water, sonicated for 30 min (42 KHz), and then shaken at 100 rpm for 24 h at RT. After centrifugation, the amount of dissolved material was determined thermogravimetrically, where a known amount of supernatant was passed through a filter paper (5-13 µm), dried at 80 ºC, and then weighed. Control experiments were performed with pure TK−2COOH and neat dextran. The studies were carried out in triplicate (Singh et al., 2023).

2.5. Determination of free carboxylic acid groups of DTKC-4

The ratio of free carboxylic acid (−COOH) groups for the DTKC-4 conjugate was determined by an acid-base back titration method (Kunc et al., 2019). First, an HCl solution (12.6 mM) in DI water was standardized using 0.01 M Na_2CO_3 solution. Then, a NaOH solution (0.069 M) was standardized using 0.1 M oxalic acid solution. Subsequently, a weighed quantity of dextran or the conjugate (10.5 mg) was dissolved in 9 mL DI water and 1 mL standard NaOH solution (0.069 M) was added. The sample was stirred for 5 min to achieve quantitative conversion of the free carboxylic acid groups to the carboxylate anions. Then, 2-3 drops of phenolphthalein were added, and the remaining hydroxide anions (OH^-) were back titrated against the standard HCl solution (12.6 mM). Neat dextran was used as the control where no −COOH groups were present. The

number of carboxylic acid groups present was calculated based on the difference in consumption of the titrant between DTKC-4 and neat dextran.

2.6. ROS responsiveness of the DTKC-4 conjugate

DTKC-4 was checked for its responsiveness to hydrogen peroxide (H_2O_2), hydroxyl radicals ($^{\bullet}OH$), and singlet oxygen ($^1O_2$). The characterization was done by ^1H NMR spectroscopy while ROS solutions were prepared in D_2O. The conjugate (10 mg) was dissolved in a glass vial containing 1 mL 100 mM H_2O_2 or 1 mL 100 mM H_2O_2 + 5 µM $CuSO_4$ ($^{\bullet}OH$), respectively, and then the solution was transferred into an NMR tube. ^1H NMR spectra were acquired at different time intervals while the conjugate dissolved in pure D_2O (1 mL) was taken as control (Xu et al., 2019).

For checking the reactivity to $^1O_2$, the water-soluble photosensitizer rose bengal (RB) was used. In 1 mL of a 1 mM RB solution in D_2O, 10 mg DTKC-4 was dissolved and the solution was then bubbled with oxygen for 15 minutes using a balloon. Then the solution was irradiated with green light (530 nm, 13.2 mW/cm^2) for different time intervals at RT and ^1H NMR spectra were taken (Lamb, & Barbas III, 2015). A non-irradiated solution was taken as control.

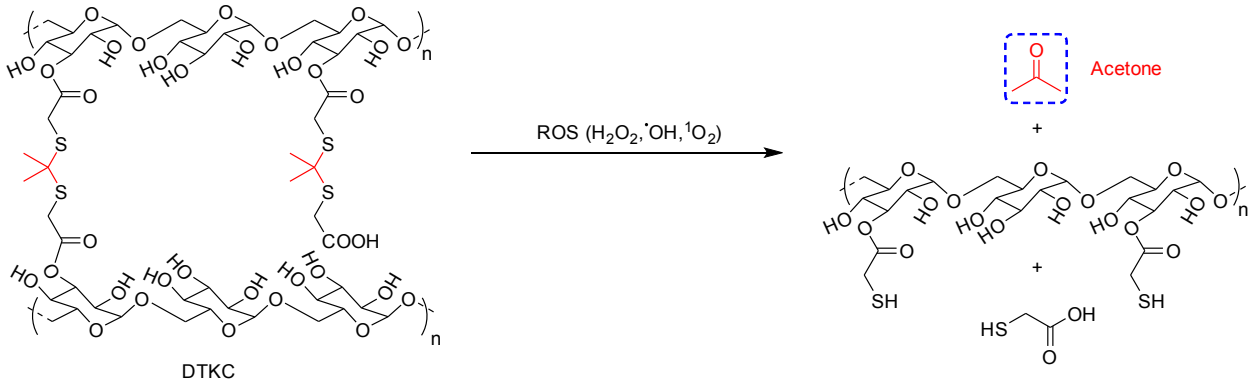

Scheme 1: Degradation of the DTKC conjugates upon exposure to ROS species, including hydrogen peroxide (H_2O_2), hydroxy radicals ($^{\bullet}OH$), and singlet oxygen ($^1O_2$).

The ROS species are known to react with the thioketal linker, leading to oxidative cleavage of the C−S bond and thereby producing acetone as a byproduct (Scheme 1), which was monitored through ^1H NMR spectroscopy at different time intervals. In all cases, the appearance of the acetone peak at 2.2 ppm and the disappearance of the thioketal peak at 1.6 ppm were monitored.

2.7. Detection of free thiols: Ellman's test

To detect the thiol-terminated products from the DTKC-4 conjugate degradation (Scheme 1), Ellman's test was performed, which is commonly used for the detection of sulfhydryl groups (–SH) in solutions. Briefly, 20 mg conjugate was dissolved in 2 mL of a 1 mM RB solution in PBS buffer (pH = 8) to get a concentration of 10 mg/mL. The mixture was purged with oxygen using a balloon to provide sufficient oxygen in the reaction mixture. Then, the solution was divided into two halves (1 mL). While the first half was irradiated with green LED light (530 nm, 13.2 mW/cm^2) for 90 min at RT, the other half was kept in the dark as control. Meanwhile, a 1 mM 5,5-dithio-bis(2-nitrobenzoic acid) (DTNB) solution was freshly prepared in PBS buffer (pH = 8). After the irradiation was complete and waiting for 15 min, 50 µL of the reaction mixture was mixed with 1 mL PBS buffer (pH = 8), and then 50 µL DTNB solution was added. The mixing time of DTNB with the reaction mixture was taken as t = 0 (min) and UV-Vis absorption spectra were taken at different time intervals (Moser et al., 2016). A control experiment was performed with the sample kept in the dark, following the same procedure. The experiments were repeated at least 3 times (n=3). For the detection of thiol-terminated products in acidic pH, the same test was performed at pH =5.1 where all the solutions were prepared at pH =5.1 and the test was performed following the same procedure.

2.8. Synthesis of the nanocarriers

The dextran-thioketal nanocarriers were synthesized by inverse miniemulsion polymerization at the droplet interface (Kuypers et al., 2015). Briefly, the dispersed phase (DP) was prepared by mixing 100 mg DTKC-4 with or without 5 mg payload (RhoB/RB/Dox) in 1 mL 0.05 M NaCl solution by gentle stirring at room temperature to form a homogeneous solution. The continuous phase (CP) was prepared by dissolving 90 mg of the polymeric surfactant Hypermer B246 in 15 mL cyclohexane in a water bath at 65 ºC until it completely dissolved. The DP was then added to the CP dropwise and the mixture was stirred at 1400 rpm for 1.5 h at RT. Then, the emulsion mixture was ultrasonicated (Branson sonifier, 450 D) at 70% amplitude (30 s on, 20 s off) for 3 min using a 3/16-inch tip while cooling it in an ice-water bath. After that, 70 µL of toluene-2,4-diisocyanate (TDI) was dissolved in 2 mL cyclohexane and added dropwise to the ultrasonicated emulsion mixture over 10 min. The crosslinking reaction of TDI with the hydroxy groups of the conjugate at the nanodroplet interface was stimulated by heating the reaction mixture at 50 ºC for 2 h. Then, the heating was stopped and the mixture was further stirred overnight at RT to

complete the reaction. Finally, the mixture was filtered through a filter paper (2 μm) to remove any large aggregates.

For transferring the NCs into water, 2 g NC solution was mixed with 10 g 0.3 wt.% SDS solution and the mixture was stirred for 1.5 h at 1400 rpm at RT in a closed vial. Then, the mixture was placed in a sonication bath (42 KHz ± 6%) for 5 min, while shaking the vial in between. Cyclohexane was evaporated by stirring the mixture in a vial with the lid kept open overnight. Finally, the redispersed sample (RD) was filtered again through a 2 μm filter paper to remove large agglomerates (if formed). The excess SDS was removed by dialysis (3.5 kDa) for a maximum of 48 h prior to characterization.

2.9. Dynamic light scattering

The hydrodynamic diameter (D_h) and polydispersity index (PDI) of the NCs were measured at 25 ºC by dynamic light scattering (DLS) using a Zetasizer Ultra from Malvern Panalytical (Malvern, UK). The average size values are reported as quadruplicate ± SD (n=4) from the independent synthesis of all nanocarriers. For cyclohexane phase samples, 20 μL NC solution was diluted with 1.5 mL cyclohexane, and Z average (intensity weighted mean hydrodynamic size) values were determined. Multi-angle dynamic light scattering (MADLS®) analysis was also performed to obtain D_h values from different angles. For the redispersed samples, a similar procedure was applied where 50 μL sample dispersion in water was diluted with 1 mL DI water. Zeta potential measurements were carried out in 1 mM KCl solution. All the measurements were carried out in triplicate and average values are reported (n=3).

2.10. Determination of the encapsulation efficiency and loading content

To determine the encapsulation efficiency (EE) of the NCs, 2 mL of RhoB, RB, and Dox-loaded NCs were centrifuged down (Sigma 3–30 K, 19776-H) at 20000 rpm for 1.5 h at 8 ºC. Then, the supernatant was collected and passed through a syringe filter (0.45 μm). The absorbance of the filtrate was measured by UV-Vis absorption spectroscopy (Nanodrop 2000c, Thermo Scientific). Depending on the payloads used, their absorbance maxima were measured and compared to the calibration curves of the respective payloads. Their concentration in the supernatant was determined (Fig. S6A-C) and the EE was calculated as

$$\text{EE (\%)} = \quad \times 100\%$$

where C_{rd} = concentration of payload used in the sample (mg/mL) and C_{sup} = concentration of payload determined in the supernatant (mg/mL). The loading content (LC) of the samples was determined according to the formula (Xu et al., 2019)

$$LC\ (\%) = \ \times 100\%$$

where $W_{payload}$ = weight of the payload in the sample (mg/mL) and W_{NC} = weight of the dried NCs (mg/mL). Measurements were carried out in triplicate (n=3) and average values were reported.

2.11. ROS responsiveness of the nanocarriers

The changes in D_h and PDI were monitored by DLS after exposure of the NCs to a ROS environment. RhoB, RB, and Dox-loaded RD NCs were stirred with 10 mM H_2O_2 at a ratio of 1:1 (v/v) in a 37 ºC water bath. At different time intervals, 100 µL of the reaction mixture was taken out for DLS measurements. The measurements were performed in triplicate and the mean ± SD (n=3) values are reported.

Detection of $^1O_2$ from the RB loaded NCs was carried out using the 1,3-diphenylisobenzofuran (DPBF) probe. A fresh 0.5 mM DPBF stock solution was prepared in EtOH prior to the experiment. In a cuvette containing 1 mL of DI water, 0.5 mL DPBF solution was mixed with 50 µL RB-NCs dispersion (t = 0), and this mixture was either irradiated with green light (530 nm, ~10 mW/cm^2) or kept in the dark. Absorbance spectra were recorded for both cases at regular time intervals while the irradiation was stopped at each minute and the spectrum was recorded immediately (Entradas, Waldron, & Volk, 2020). To check the photobleaching of DPBF, another control experiment was conducted by irradiating a DPBF-only solution of the same dilution and recording the absorbance spectra. All experiments were repeated at least 3 times (n≥3).

2.12. Payload release studies

The cumulative release (%) experiments were carried out with RhoB (*ca.* [RhoB]= 62.5 µg/mL) and Dox (*ca.* [Dox] = 67.5 µg/mL) loaded NCs. In general, 2 mL sample dispersion was mixed with 1 mL H_2O_2 (1 mM or 10 mM) solution in a dialysis bag (MWCO 3.5 kDa) and the bag was immersed in 15 mL H_2O_2 solution (1 mM or 10 mM) at 37 ºC in a water bath while stirring at 100 rpm. After predetermined time intervals, 2 mL outside release medium was replaced with 2 mL fresh H_2O_2 solution. To assess the release of the payloads in a medium containing relevant biomolecules, ions, etc., the cumulative release of payloads was also evaluated in a conditioned

culture medium (CCM), which was generated by incubating OSCC cells and collecting it after two days. A 20% CCM (v/v) was used to avoid clogging of the dialysis bag pores and cumulative release was performed similarly as mentioned before. The control experiment was performed as a continuous release without H_2O_2 conditions. The absorbances of the released media were measured by UV-Vis absorption spectroscopy at well-defined time intervals and their concentrations were calculated from the respective calibration curves (supplementary material, Fig. S6A, C). Cumulative release (%) was calculated according to the formulae reported in the literature (Chen et al., 2019). The measurements were carried out in triplicate and mean ± SD (n=3) values are reported.

The light responsive release of RB from the NCs was also carried out. First, quenching of RB (100 µg/mL) due to light irradiation was checked for different time intervals. 2 mL sample dispersion (*ca.* [RB] = 59.25 µg/mL) was irradiated (530 nm, ~13.2 mW/cm^2) for 10, 20, 30, and 40 min, respectively, and transferred into dialysis bags. The bags were then incubated in 15 mL DI water for 24 h at 37 ºC. A control experiment was performed with a non-irradiated sample, following a similar procedure. The released RB dye intensity was measured by UV-Vis absorption spectroscopy and the concentrations were determined from the calibration curve of RB (supplementary material, Fig. S6B).

2.13. *In vitro* experiments

2.13.1. Cell culture

The human OSCC cell line UM-SCC-14C (CLS cell lines service, Germany, CVCL 7721) was cultured in Dulbecco's Modified Eagle Medium/Nutrient Mixture F-12 (DMEM/F-12) (Gibco™, Thermo Fisher Scientific) supplemented with 5% heat-inactivated fetal bovine serum (FBS) and 1% penicillin/streptomycin and maintained in an incubator preserved at 37 ºC in a humidified atmosphere with 5% CO_2.

2.13.2. Cell viability assay

Cells were seeded at a density of 15x10^3 cells/cm^2 and allowed for adherence. Next, the cells were incubated over a period of 24, 48, and 72 h with different concentrations of NCs diluted in a culture medium. At given time points, the AlamarBlue protocol was performed according to the manufacturer's instructions. Fluorescence intensity was measured using the CLARIOstar® PLUS

plate reader (BMG Labtech, The Netherlands) at a wavelength of 540/590 nm. Data were normalized to the negative control. Outliers were detected and statistical analyses were performed using GraphPad Prism 9. The statistical tests used are Two-way ANOVA followed by Dunnett's multiple comparisons test.

2.13.3. Cellular uptake studies

Cells were seeded at a density of $15x10^3$ cells/cm² on glass coverslips. Following overnight adherence, cells were incubated with NCs and then fixed using 4% paraformaldehyde (PFA) for 20 min at RT. Next, the cells were incubated with 1:200 wheat germ agglutinin AlexaFluor 647 (WGA647) for 10 min followed by nuclear staining using 4′,6-diamidino-2-phenylindole (DAPI). Cells were mounted with Fluorescence Mounting Medium (Dako) on microscopic slides for imaging with the LSM900 confocal microscope (Zeiss). Images were acquired in z-stack mode and processed using the ZEN Blue software (Zeiss).

2.13.4. Flow cytometry

Cells were seeded at a density of $23x10^3$ cells/cm^2 and allowed for overnight adherence. Following, the cells were incubated with 100 µg/mL of NCs for an incubation period of 2, 4, 6, and 24 h. The cells were collected and stained using the Zombie NIR viability dye (BioLegend) and centrifugation was performed at RT for 5 min at 2000 rpm. Next, a total of 10 x 10^3 events were recorded using the LSRFortessaTM (BD Biosciences) Flow Cytometer. The FlowJo software was used to gate the cell population in a plot of FSC versus SSC. Cell debris and doublets were excluded, and a histogram from the PE channel was created to calculate the percentage of Rhodamine B-positive cells. Statistical analyses included a One-way ANOVA followed by Dunnett's multiple comparisons test and were performed using GraphPad Prism 10.

2.14. Analytical methods

^{1}H and ^{13}C NMR spectra were measured on a 400 MHz nuclear magnetic resonance spectrometer (Varian Inova) with a sample concentration of 10 mg/mL in D_2O (4.79 ppm) or 60 mg/mL in DMSO d_6 (2.50 ppm), using a 5 mm four-nucleus PFG probe. The chemical shift scale was calibrated relative to TMS (0 ppm). Unless stated otherwise, all measurements were performed at room temperature. Acquisition parameters used for the ^{1}H measurements were: a spectral width of 6.4 kHz, a 90° pulse length of 6.4 µs, an acquisition time of 2.5 s, a recycle delay time of 10 s,

and 32 accumulations. For the HETCOR (heteronuclear chemical shift correlation) 2D NMR measurements, the delay times were optimized to observe direct ^{1}H- ^{13}C couplings [1J(C, H) = 140 Hz]. The spectral width was set to 3600 Hz and 27000 Hz in F1 and F2, respectively and spectra were accumulated with a relaxation delay of 7.5 s, an acquisition time of 0.2 s, 112 scans, and 72 FID increments in F1 and 5K data points in F2. For the HMBC (heteronuclear multiple bond correlation) 2D NMR measurement, the delay times were optimized using a J-value of 7 Hz to observe long-range ^{1}H- ^{13}C couplings. The spectral width was set to 22000 Hz and 5200 Hz in F1 and F2, respectively and spectra were accumulated with a relaxation delay of 2 s, an acquisition time of 0.2 s, 384 scans, and 192 FID increments in F1 and 974 data points in F2. For the ^{13}C measurement (DTKC-4), 20 mM chromium(III) acetylacetonate was added as a relaxation reagent. Acquisition parameters used were: a spectral width of 25.1 kHz, a 90° pulse length of 10.8 µs, an acquisition time of 0.8 s, a recycle delay time of 6 s, and 50.000 accumulations (95 h acquisition. Solid-state ^{13}C NMR was carried out according to a previous report (Seneca et al., 2020). Elemental analysis was performed using a Thermo Electron Flash EA1112 elemental analyzer (ThermoFisher Scientific, Waltham, USA). Calibration was carried out using BBOT ((2,5-bis(5-*tert*-butyl-benzoxazol-2-yl)thiophene) (Thermo Scientific). The powders were weighed and measured as such. Samples were measured at least in triplicate. ATR-FTIR spectroscopic measurements were carried out using a Bruker Invenio S spectrophotometer. The spectra were recorded in the range 600–4000 cm^{-1} with a resolution of 16 cm^{-1}, by directly placing a lyophilized or dried sample in the spectrophotometer. Morphological studies of the NCs were done by TEM imaging using a Tecnai Spirit TEM operating at 120 kV (FEI Company, Hillsboro, Oregon, USA) with an Olympus-SIS MegaView G2 CCD camera. The diluted samples were drop casted and air dried on a TEM grid (formvar foil upon copper grids, Electron Microscopy Sciences). No additional staining was performed for imaging.

3. Results and discussion

3.1. Synthesis of the thioketal linker and the dextran-thioketal conjugates

Synthesis of the thioketal linker (TK-2COOH) was carried out by a simple acid-catalyzed reaction of a ketone (C=O) with a thiol (− SH) (Fig. 1(1)) and the linker molecule was characterized by ^{1}H and ^{13}C NMR spectroscopy (supplementary material, S1). The dextran-thioketal conjugates were then synthesized by Steglich esterification (Lian et al., 2017) of the −COOH and −OH groups from the thioketal and dextran, respectively. The molar ratio of TK-2COOH to the anhydrous glucose unit (AGU) of dextran was varied (0.5×, 1×, 1.3×) under different reaction conditions (supplementary material, S2) to increase the thioketal content in the conjugates, which were characterized by ^{1}H NMR and FTIR spectroscopy (Fig. 2). First, the characteristic proton signals from the glucose ring protons of the conjugate were assigned to 4.95 (H-1), 3.96 (H-6b), 3.88 (H-5), 3.70 (H-3, H-6a), and 3.54 (H-2, H-4) ppm in the ^{1}H NMR spectra (Zeini et al., 2021). The methyl proton signal from the thioketal group of a typical conjugate appeared around 1.6 ppm (H-9 + 9′ at 1.32-1.84 ppm, 6H, $-(C\underline{H_3})_2C\text{-}S-$) (Fig. 2A). Peak broadening was observed for all the conjugates due to the deceleration of molecular tumbling caused by the increase in molecular weight due to crosslinking. Such observation is common for high molecular weight biopolymers. Kunc et al. for instance also observed peak broadening when succinic anhydrides were attached to dextran to form polycarboxylated dextran (Kunc et al., 2019). The methylene protons (4H) of TK-2COOH, were found to be situated around 2.90 ppm. Some residual traces of EDC at 1.99 and 1.17 ppm (denoted by * in Fig. 2A) and DMAP at 8.42 and 6.89 ppm were still present in the conjugate. To further characterize the proton as well as carbon peaks of the conjugate, ^{1}H–^{13}C 2D HETCOR NMR spectra were conducted for the pure linker (S2.6), dextran (S2.7), and the DTKC conjugate (Fig. 2B). Based on the ^{1}H–^{13}C correlations in the HETCOR spectrum of the conjugate, the carbon signals from the dextran α-(1 → 6)-linked glucose units are assigned as: 68.0 ppm (C-6), 72.0 ppm (C-4), 72.6 ppm (C-5), 74.0 ppm (C-2), 75.9 ppm (C-3), 100.2 ppm (C-1). The CH_3 and CH_2 peaks of the linker appear at 32.3 ppm and 45.3 ppm, respectively. Furthermore, the esterification site of the linker to the glucose ring was investigated by ^{1}H–^{13}C 2D HMBC spectroscopy (Heteronuclear Multiple Bond Correlation spectroscopy). A correlation spot (^{3}J-coupling) between the carbonyl carbon at around 172 ppm and the H-3 proton of the glucose ring indicates an esterification of the linker with the C-3 hydroxy group of the glucose ring (Fig. 2C).

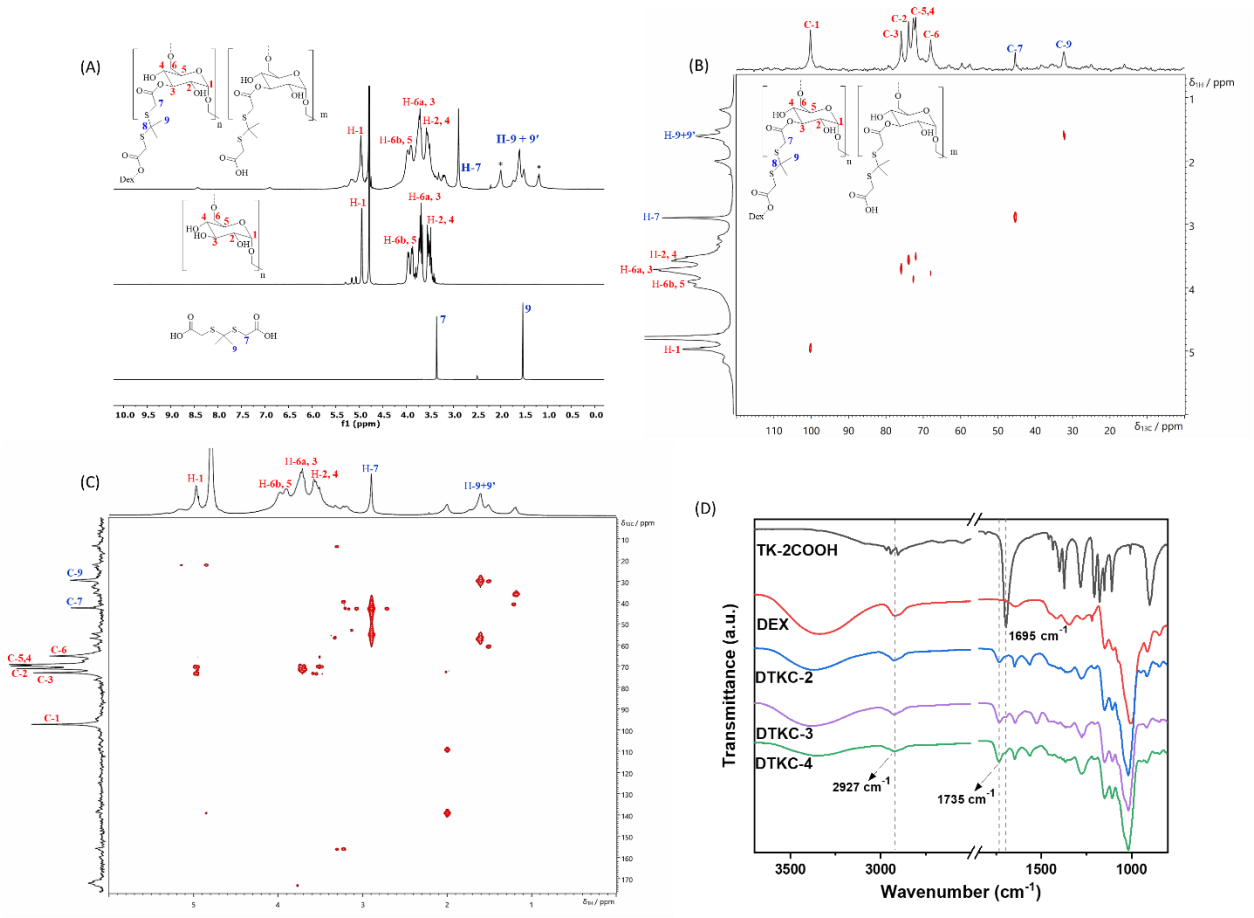

Fig. 2: Characterization of the dextran-thioketal conjugates. (A). Stacked ^{1}H NMR spectra of thioketal (TK-2COOH), dextran, and a typical dextran-thioketal conjugate (DTKC). The ^{1}H NMR spectrum of TK-2COOH was taken in DMSO-d_6, whereas the dextran and DTKC spectra were obtained in D_2O ('*' denotes the peaks of remaining EDC at 1.99 and 1.17 ppm). (B). The ^{1}H–^{13}C 2D HETCOR NMR spectrum of the DTKC conjugate and (C). The ^{1}H–^{13}C 2D HMBC NMR spectrum of the conjugate in D_2O. (D). ATR-FTIR spectra of TK-2COOH, dextran (DEX), and the DTKC-2, DTKC-3, and DTKC-4 conjugates.

Optimization of the esterification reaction was carried out by increasing the molar feed ratio of TK-2COOH: AGU to 0.5, 1, and 1.3 (Table S1) under different reaction conditions and the degree of substitution (DS_{TK}) was quantified by ^{1}H NMR (Fig. S2.1-S2.5). When 0.5 equivalents of TK-2COOH were used at RT or 45 ºC, the DS_{TK} increased from 3% (DTKC-1) to 8% (DTKC-2). Increasing the TK-2COOH amount to 1 equivalent resulted in a DS_{TK} of 14% (DTKC-3) for a reaction of 24 h at 45 ºC. Further increase of the TK-2COOH amount to 1.3 equivalents resulted in a DS_{TK} of 23% (DTKC-4) for a reaction of 48 h at 45 ºC. The conjugates were further characterized by ATR-FTIR spectroscopy (Fig. 2D). For all the conjugates, ester bonds were found at 1735 cm^{-1} in accordance with literature (Su et al., 2017). The presence of a small peak at 1695 cm^{-1} could be attributed to remaining unreacted -COOH groups in the conjugate, i.e. TK-

2COOH linkers that are esterified with dextran at one end only. These are more prominently observed for DTKC-3 and 4 whereas the C-H stretching vibrations in the 2850-2970 cm^{-1} region are from the CH_2 and CH_3 groups of the linker as well as from the C-H bonds of the sugar ring, as also observed for the native and functionalized dextran (Nikonenko et al., 2000).

Since the thioketal linker is relatively hydrophobic and crosslinking reduces chain mobility of the polymer, a decrease in solubility of the conjugate with increasing substitution level is to be expected. Solubility of the thioketal linker molecule was determined to be 15.7 ± 3.2 mg/mL in water at RT (23 ºC), whereas neat dextran showed high solubility (>0.459 g/mL). DTKC-2 and DTKC-3 conjugates showed a solubility >150 mg/mL, but DTKC-4 showed a reduced solubility of 120.3 ± 5.1 mg/mL. Therefore, a gradual decrease of the solubility with an increase of the thioketal content in the polymer was realized.

From the nanocarrier perspective, a higher degree of thioketal content in the conjugate can enable a faster release of the payloads, whereas a good water solubility of the materials in the dispersed phase of the nanocarrier formulation is also important for increasing the DTKC concentration to improve the polymeric shell thickness for safe encapsulation of the payloads as well as for the colloidal stability of the emulsions. Therefore, the DTKC-4 was selected as the optimal conjugate for nanocarrier synthesis, since it has the highest thioketal substitution and could also be dissolved homogeneously in DI water, NaCl solution, PBS buffer, and in the presence of different payload molecules.

For quantifying the conjugation in DTKC-4, besides the DS_{TK} of 23% obtained via ^{1}H NMR, the degree of substitution (DS) was also determined via the carbon atoms of the carbonyl groups ($DS_{C=O}$) and the amount of sulfur ('S') by ^{13}C NMR and elemental analysis, respectively. ^{13}C NMR of the conjugate (Fig. S3) showed a total $DS_{C=O}$ of 31% and the presence of two carbonyl peaks between 168 and 174 ppm, probably corresponding to C=O carbons from linker molecules that are crosslinked (two-sided esterification) and COOH carbons from linker molecules that are esterified at a single site only. The intensity distribution of these two peaks suggests that 61% of the attached linkers are esterified at both ends with the glucose ring (Fig. S3). The presence of mono-esterified linkers was also determined quantitatively by an acid-base back titration method (Kunc et al., 2019). Neat dextran (blank) and DTKC-4 were titrated separately and their difference in consumption of HCl could be attributed to the free N_{COOH} groups, which was

calculated to be 0.1 mmol/g conjugate. Elemental analysis showed a 'S' content of 2.48 mmol/g conjugate (Table S2) and DS_s was calculated to be 27% (Fig. S4). Comparing all three different techniques, an average $DS_{average}$ of 27 ± 4% could be established for DTKC-4.

3.2. ROS responsiveness of the conjugate DTKC-4

The dextran conjugate was tested for its reaction with H_2O_2, $^{\cdot}OH$, and $^1O_2$ independently to evaluate the degradation products. It is well known that ROS reagents induce oxidative cleavage at the C−S bond of the thioketal, eventually leading to the generation of acetone and other products (Liu, & Thayumanavan, 2020). When the conjugate was incubated with 100 mM H_2O_2 or 100 mM H_2O_2 + 5 μM $CuSO_4$ ($^{\cdot}OH$) for different time intervals, a time-dependent gradual appearance of acetone at 2.2 ppm and disappearance of the thioketal proton signal around 1.6 ppm was observed by ^1H NMR (Fig. 3A-B). The conjugate was more reactive with $^{\cdot}OH$ radicals than with only H_2O_2 as can be observed from the strong diminishment of the methyl peak between 1.32-1.84 ppm (Fig. 3B) within 24 h. Longer incubation (120 h) of the conjugate with H_2O_2 showed a better effect on thioketal protons decrement and acetone generation (Fig. S5), suggesting slow degradation of the conjugate.

To assess the reaction with $^1O_2$, the conjugate was tested with RB as the photosensitizer to produce $^1O_2$ *in situ* upon green light irradiation. RB is a xanthene photosensitizer and is an excellent water-soluble dye with a good singlet oxygen production quantum yield at RT (Entradas, Waldron, & Volk, 2020). After irradiation of the conjugate with RB for different time intervals, ^1H NMR spectra were taken in D_2O and a time dependent acetone generation was detected (Fig. 3C). In the control experiment where no irradiation was performed, no sharp acetone peak was found. This confirms the reactivity of the conjugate with $^1O_2$. Overall, the conjugate exhibited greater reactivity toward $^{\cdot}OH$ radicals compared to H_2O_2, as evidenced by the faster reduction in thioketal CH_3 peak intensity as a function of the incubation period (Table S3). The reactivity toward $^1O_2$ was comparable to that toward $^{\cdot}OH$ radicals, at least for 1h; however, photobleaching of RB limits the evaluation of the ROS production ability over longer periods (Table S3).

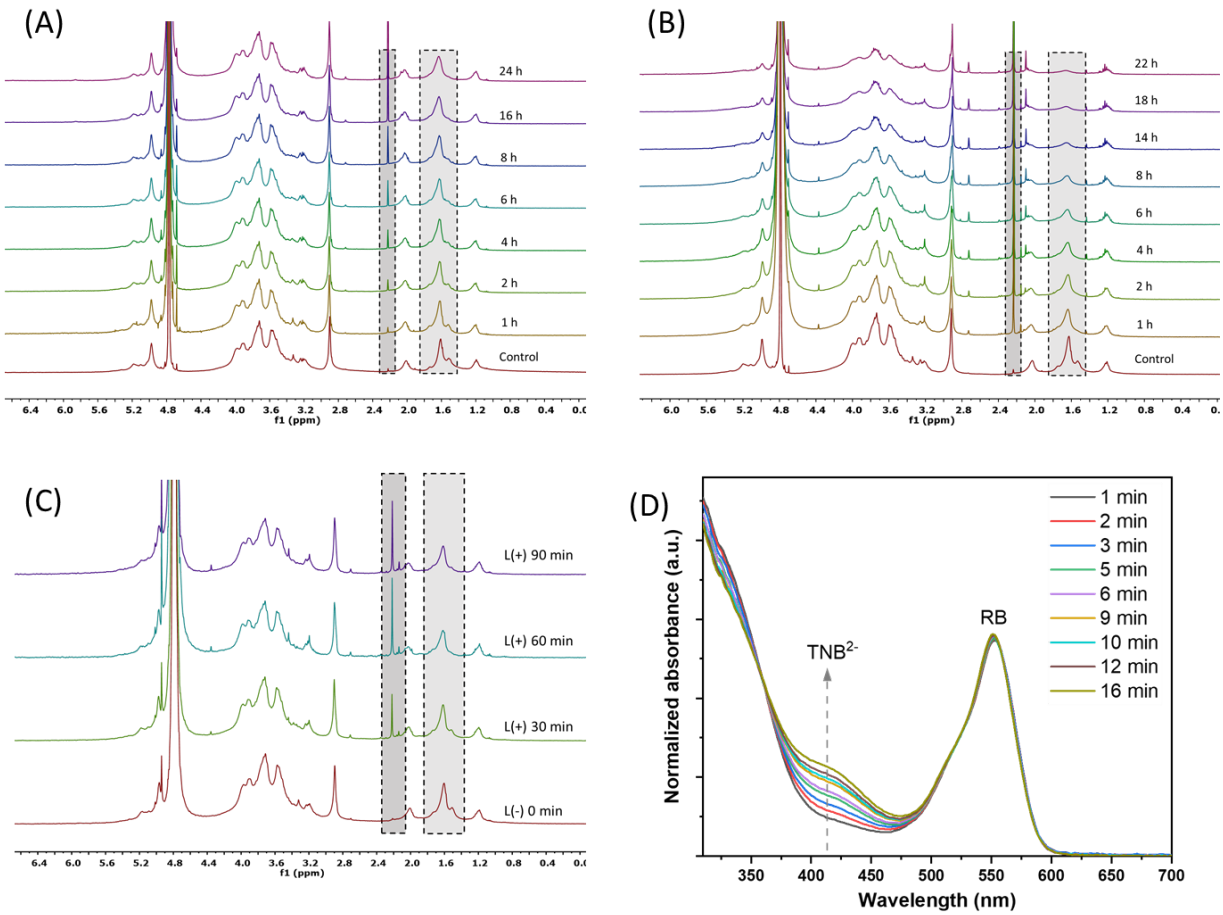

Fig. 3: Characterization of the ROS responsiveness of the dextran-thioketal conjugate. (A). ^{1}H NMR spectra of the DTKC-4 conjugate after incubation with 100 mM H_2O_2 in D_2O. (B). ^{1}H NMR spectra of DTKC-4 after incubation with 100 mM H_2O_2 + 5 µM $CuSO_4$ ($^{\cdot}$OH) in D_2O (C). ^{1}H NMR spectra of the conjugate + rose bengal (RB) after irradiation with green light (530 nm) for different time intervals. (D). UV-Vis absorption spectra of the light-irradiated reaction mixture containing DTNB (Ellman's reagent).

Detection of thiol degradation products from the conjugate was carried out qualitatively by Ellman's method (Moser et al., 2016). 5,5′-Dithio-bis(2-nitrobenzoic acid) (DTNB) is known as Ellman's reagent and is commonly used for the detection of free thiols from peptides and proteins (Rudyk & Eaton, 2014). The sulfhydryl groups (−SH) act as a nucleophile and attack the -S-S- bond of DTNB to form a mixed disulfide and a TNB anion, which gives rise to an absorption peak at 412 nm. In a study by Cathell et al., DTNB was used to study thiol modification after conjugating different thiol containing acids with chitosan in PBS buffer at pH 8 (Cathell et al., 2008). Detection of thiols was also reported in a system where RB was used as a $^1O_2$ generator and did not affect thiol detection (Kukreja et al., 1991). Following a similar procedure, first a reaction mixture (DTKC-4 + RB) was irradiated with green light to produce degradation products

and then this was mixed with DTNB solution (t = 0; PBS buffer, pH = 8). UV-Vis absorption spectra were taken at different time intervals after mixing (Fig. 3D). With an increase in time, the DTNB peak at 316 nm decreased and the TNB^{2-} peak appeared at 412 nm, with a clear isosbestic point, while the peak at 550 nm from RB remained unaffected. However, for the control experiment with a non-irradiated reaction mixture, a weak peak of TNB^{2-} was also observed (Fig. S7.1). This false positive response can arise due to the hydrolysis of DTNB since DTNB is known to undergo hydrolysis at higher pH and elevated temperature (pH = 8) (Winther and Thorpe, 2014). Nevertheless, upon comparing the absorbance maxima at 412 nm for both cases after 16 minutes of mixing with DTNB, absorptivities A_L = 0.285 (light irradiated) and A_C = 0.142 (control) were obtained. The extra absorbance (ΔA_{L-C} = 0.143) from the irradiated sample could be attributed to the reaction of DTNB with thiols from the reaction mixture. To ascertain the presence of thiol terminated degradation products, the same test was performed at pH =5.1 to avoid the hydrolysis of DTNB, following an exactly similar procedure. In this case, the light irradiated mixture showed a gradual appearance of a TNB^{2-} peak at 412 nm (Fig. S7.2) whereas in the control experiment (non-irradiated, pH =5.1), no change at 412 nm was observed (Fig. S7.3). This confirms the evolution of the thiol terminated degradation products upon irradiation of the DTKC-4 conjugate with the photosensitizer RB. A similar test could not be performed with reaction mixtures from H_2O_2 and $^{\bullet}OH$ due to the fact that the presence of H_2O_2 can oxidize thiols (−SH) to sulfonic acids ($-SO_3H$) or a disulfide bond, thereby making free thiols unavailable (Van Bergen, Roos, & De Proft, 2014). Regardless, summing up all the different approaches to assess the ROS responsiveness, it can be concluded that the dextran conjugate is responsive to all the individual ROS species H_2O_2, $^{\bullet}OH$, and $^1O_2$.

3.3. Synthesis and characterization of the nanocarriers

Inverse miniemulsion polymerization at the droplet interface was used to prepare the NCs using water and cyclohexane as the dispersed and continuous phases, respectively. Prior to the nanocarrier synthesis by miniemulsion, the stability of the thioketal bonds in the DTKC-4 conjugate was checked by NMR spectroscopy after the ultrasonication step and was found to be unaffected under the tested conditions (Fig. S8). In here, the organic phase contains the polymeric surfactant and the aqueous phase contains DTKC-4 and the different payloads. Nanoemulsion droplets were created by ultrasonicating the emulsion mixture and then a crosslinker (TDI) was introduced in the organic phase to react at the interface of the droplets (Fig. S9.1). Finally, the

NCs were transferred into an aqueous phase containing SDS and are denoted further on in the text as redispersion (RD). The crosslinking by TDI is crucial to form a polymeric shell at the interface of the droplets as well as to provide stability to the emulsion droplets which further prevents the nanocarriers from disassembly while transferring from the organic to the water phase (RD) and encapsulating the payloads in the inner aqueous core. Then the redispersed samples were dialyzed to remove excess SDS. Three different water-soluble drugs – RhoB, RB, and Dox – were selected as model payloads, and the NC dispersions were characterized.

Table 1. Overview of the hydrodynamic diameter (D_h), polydispersity index (PDI), and zeta potential of the DTKC-4 NCs with or without different payloads as measured using DLS at 25 °C. The drug loading content (LC) and encapsulation efficiency (EE) are also presented for the different NCs.

Payload	D_h (nm) (cy)	PDI	D_h (nm) (water)	PDI	EE* (%)	LC* (%)	Zeta potential (mV)
-	150 ± 14	0.1 ± 0.04	165 ± 21	0.2 ± 0.04	-	-	-12.1 ± 1.8
RhoB	181 ± 22	0.14 ± 0.09	193 ± 23	0.29 ± 0.1	85 ± 4.8	11 ± 1	-11.3 ± 3
RB	179 ± 15	0.1 ± 0.08	193 ± 26	0.29 ± 0.1	79 ± 6.5	10.5 ± 2	-16.2 ± 2.8
Dox	173 ± 24	0.17 ± 0.04	173 ± 24	0.23 ± 0.04	91 ± 4.3	11.3 ± 1	-12 ± 3

cy = cyclohexane. Zeta potential values were obtained after 24 h dialysis. '*' denotes the values for mean ± SD (n=3), while the other values are represented as mean ± SD (n=4).

First, the colloidal features of the NCs were studied by DLS to check their D_h, PDI, and zeta potential (Table 1 and Fig. 4A-C). In general, D_h lies between 150 and 181 nm in cyclohexane with PDI values from 0.1 to 0.17. Transferring the NCs into the water resulted in D_h and PDI increments. This is in line with our previously reported synthesis of pure dextran nanocapsules, where RhoB was used as the model payload (Nayak et al., 2023). The size increment could be attributed to swelling of the NCs, which is common for dextran due to its hydrophilicity (Alkanawati et al., 2020). Upon comparing the EE, the highest value of *ca.* 91 ± 4.3% was found for the Dox loaded NCs, while the overall EE was in the range of 79–91%. LC values of the NCs were found in between 10.5 and 11.3% (Table 1), comparable to the prodrug conjugates (Ding et

al., 2023; Sun et al., 2017). The NCs were stable for at least 3 weeks when stored at 4 ºC without a significant change in D_h or PDI, indicating the absence of aggregation and/or precipitation.

The different NCs (RhoB, RB, Dox, and non-loaded DTKC-4 NCs) were characterized by TEM for morphological analysis. All the NCs exhibited a nanocapsule morphology in the TEM characterization (Malzahn el at. 2014; Schlegel et al.,2018) where the thin polymeric shell appeared as crumpled structures (Fig. 4D-F, Fig. S9.2). Such capsule morphology was observed previously with neat dextran NCs and crosslinked gelatin capsules, both obtained by interfacial polymerization in the inverse miniemulsion using the toluene diisocyanate (TDI) as a cross-linker (Nayak et al., 2023; Bacher et al., 2019). Furthermore, similar morphology was also reported by Alkanawati et al., where the nanocapsules were obtained using the interfacial bio-orthogonal crosslinking between the ketone/oxidized (aldehyde) functionalized dextran and a hydrazide crosslinker (Alkanawati et al., 2020). The samples exhibited low contrast while imaging and appeared smaller in size as compared to the DLS results, which can be attributed to the drying effect of the NCs on the TEM grid. Irrespective of the presence or absence of the payload, there is no characteristic difference between the different NC samples.

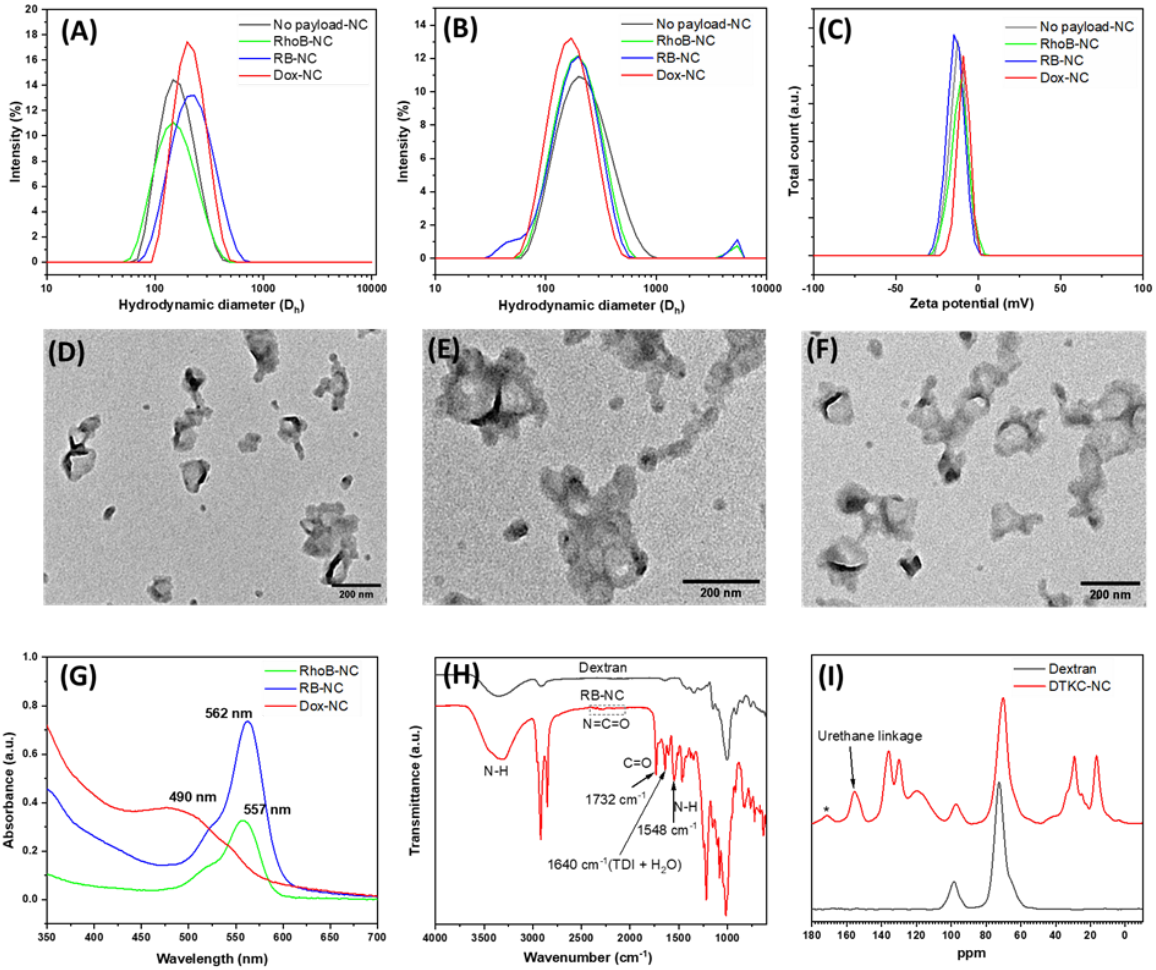

Fig. 4: Characterization of the nanocarriers. DLS data of non-loaded and RhoB, RB, and Dox loaded nanocarriers in cyclohexane (A) and in water (B) (D_h = hydrodynamic diameter). (C) represents the corresponding zeta potentials of the NCs. Representative TEM images of the nanocarriers where (D) shows the RhoB loaded NCs, (E) the RB loaded NCs, and (F) the Dox loaded NCs. (G) UV-Vis absorption spectra of the nanocarriers with different payloads. (H). Representative FTIR spectra of dextran and dried RB loaded NCs. (I). ^{13}C solid-state NMR spectra of pure dextran and dried DTKC-4 NCs without any payload (* denotes the ester signal at 171 ppm).

UV-Vis absorption spectra of the NCs are shown in Fig. 4G. A bathochromic shift in the absorption maxima (λ_{max}) of the dyes/drugs was observed after encapsulation in the NCs. To analyze the interfacial crosslinking of the −NCO groups of TDI with the −OH groups from the conjugate, ^{13}C solid-state NMR and FTIR spectroscopy were employed (Fig. 4H-I). A representative FTIR spectrum of the RB-NCs is shown in Fig. 4H, where the strong carbonyl peak at 1732 cm^{-1}, the -NH stretching peak at 3286 cm^{-1}, and the NH bending peak at 1548 cm^{-1} were observed, in accordance with the literature (Seneca et al., 2020). In a control experiment, where no payload was used, similar peaks were evidenced from the DTKC-NCs (Fig. S9.3).

Further, the peak at around 1640 cm^{-1} indicates the side reaction of TDI with water (Jagielski et al., 2007). Complete consumption of the −NCO groups of TDI was indicated by the nearly flat baseline at 2276 cm^{-1}. ^{13}C solid-state NMR of the non-loaded NCs further indicated the urethane linkage at 155 ppm (Fig. 4I). The peak at around 171 ppm could be attributed to the ester bonds arising from the conjugate DTKC-4. Thus, it was concluded that the interfacial crosslinking at the droplet interface was successful and nanocapsules with different payloads were obtained with good EE, LC, and colloidal stability.

3.4. ROS responsiveness of the nanocarriers

The NC dispersions with RhoB, RB, and Dox were incubated with 10 mM H_2O_2 and their change in D_h and PDI was monitored by DLS at different time intervals (Fig. 5A and Fig. S10). In general, for all the NCs, D_h and PDI increased with time. This could be attributed to NC aggregation, destruction of NC morphology, and swelling due to the degradation of the conjugate by H_2O_2. The effect was most pronounced for the RhoB loaded nanocapsules, which attained a maximum D_h of 735 nm and PDI of 0.4 within 30 h of incubation. At the same time, the D_h for the RB and Dox loaded samples was 440 and 353 nm with a maximum PDI of 0.31 and 0.37, respectively (Fig. 5A). Zhang et al. reported crosslinked nanoparticles from oligo(ethylenimine) and thioketal linkages and observed an increment in D_h and PDI up to 1500 nm and 0.48, respectively, after exposure to a strength of 400 mM + 1.6 µM $CuCl_2$ of Fenton's reagent (Zhang et al., 2019).

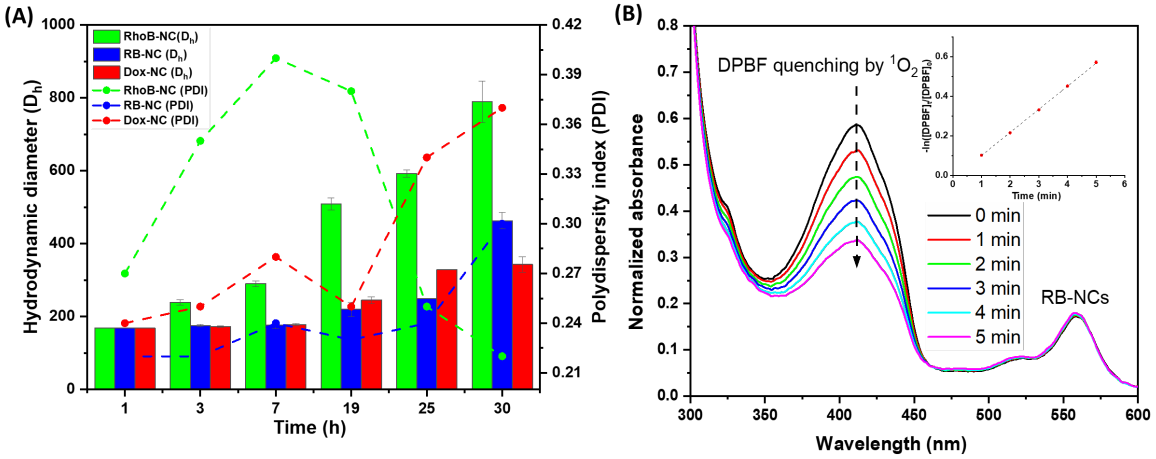

Fig. 5: Characterization of the ROS responsiveness of the nanocarriers with different payloads. (A). Time-dependent change in hydrodynamic diameter (D_h) and polydispersity index (PDI) of the NCs loaded with RhoB, RB, and Dox, after incubation with 10 mM H_2O_2 ROS solution (D_h is represented as mean ± SD

values, SD set as y-axis error, n=3). (B). The production of $^1O_2$ from RB-loaded NCs was analyzed by colorimetry using DPBF as a $^1O_2$ detection agent. A reaction mixture containing DPBF (0.5 mM) and RB-loaded NCs was irradiated with green LED light (530 nm, 10 mW/cm^2), and UV-Vis absorption spectra were taken for 0 to 5 minutes at each minute. Inset graph represents -In ($[DPBF]_t/[DPBF]_0$) vs time (t, min) plot.

The nanocarriers were further tested for singlet oxygen production from the RB loaded NCs to test the hypothesis of the cascade reaction, where singlet oxygen species produced via irradiation of the photosensitizer can subsequently cleave the TK linker. To check the $^1O_2$ production from RB after encapsulation, the NC dispersion in water was mixed with a 1,3-diphenylisobenzofuran (DPBF) solution and irradiated with green light. Light irradiation to the mixture is expected to afford $^1O_2$, which can be quantified by the decrease in the absorbance/fluorescence of DPBF. UV-Vis absorption spectra were taken after each minute of irradiation (530 nm, ~10 mW/cm^2) for 5 minutes and are presented in Fig. 5B. The decrement in the peak maximum at 411 nm corresponds to the quenching of DPBF with a calculated rate constant 1.94×10^{-3} sec^{-1} (inset Fig. 5B) (Wang et al., 2019). Alternatively, quenching of DPBF can happen due to photodegradation rather than $^1O_2$ capture. Thus, a control experiment was performed with only DPBF (without RB-NCs) and this solution was irradiated independently at the same dilution while maintaining the identical irradiation parameters. Only 6% DPBF intensity quenching was observed after 5 minutes, compared to the quenching in the presence of RB-NCs (Fig. S11.1). In another control experiment, the non-irradiated RB-NCs and DPBF mixture were studied by UV-Vis absorption spectroscopy, where virtually no change in DPBF absorbance was monitored (Fig. S11.2). These experiments indicate that the DPBF quenching is mainly caused by the produced $^1O_2$ and a minimal amount (6%) due to photobleaching. Hence, the $^1O_2$ production ability of RB in an aqueous environment, even after encapsulation into the NCs, was successfully confirmed.

3.5. Payload release studies

Since ROS solutions have oxidizing abilities, at first the degradation of the dye/drug (RhoB and Dox) in the experimental conditions used to study the cumulative release was checked by testing the respective payloads in 1 mM and 10 mM H_2O_2 environments (Fig. S12.1). Under the tested conditions, the absorbances of RhoB and Dox were only slightly affected until 24 h but decreased more significantly after 48 h of incubation. Incubation with 100 mM H_2O_2 resulted in more quenching within 24 h for both cases. Therefore, the release was only checked for rather low molar concentrations of H_2O_2 (Xu et al., 2017; Xu et al., 2019).

A sample dispersion of RhoB-NCs in a dialysis bag (MWCO = 3.5 kDa) was incubated with H_2O_2 solutions at 37 ºC and the release of RhoB outside the bag was plotted as a cumulative release (%) in Fig. 6A. On changing the H_2O_2 strength from 1 to 10 mM, the release proceeded faster, releasing a maximum of ~21% and ~30% of dye to the outside medium, respectively, after 30 h of incubation. In the control experiment where no H_2O_2 was used, *ca.* 7.8% dye release was observed after 24 h of incubation. Photographs of the release media taken after 30 h are shown in the inset of Fig. 6A.

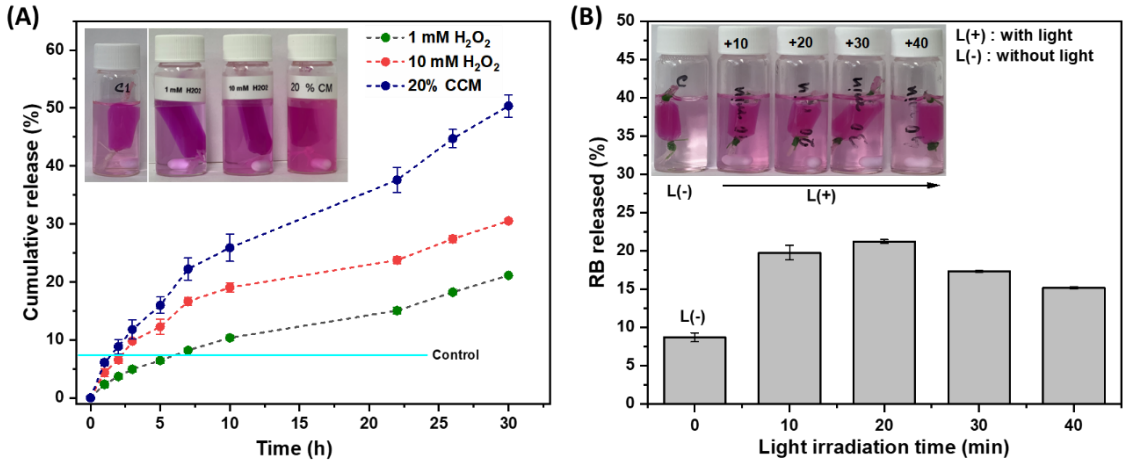

Fig. 6: Characterization of payload release under ROS conditions. The cumulative release profile of RhoB (A) from DTKC-4 NCs under ROS conditions of 1 mM H_2O_2, 10 mM H_2O_2, and 20% OSCC cell conditioned culture medium (CM) at 37 °C for 30 h (mean ± SD values, SD set as y-axis error, n=3). Milli-Q water was used as control. In the inset, photographs of the vials taken after 30 h are shown. (B) RB release (%) from the NCs after light irradiation for 10, 20, 30, and 40 minutes (mean ± SD values, SD set as y-axis error, n=2). In the inset, photographs of the release vials taken at the respective time points are shown.

To study the release of the payloads in a relevant cellular environment that contains biomolecules, ions, etc., the cumulative release was evaluated in a conditioned culture medium (CCM) which was collected after incubating the culture medium with the OSCC cancer cells (Wu et al., 2020). Interestingly, in the 20% CCM (v/v), a dye release of 50.4 ± 1.9% within 30 h was observed. As CCM likely contains a mixture of proteins, oxidative species, enzymes, and other (sub)cellular components, it is not straightforward to attribute this effect to a specific factor(s) that can influence the release of the payload. However, to ascertain the extent of ROS responsive release (as OSCC cells produce excess ROS) (Kesarwala, Krishna, & Mitchell, 2016), two control experiments were performed with DTKC-NCs and pure dextran NCs (Dex-NCs) in 20% CCM as well as in 20% non-cell incubated blank medium (BM). First, pure dextran NCs (Dex-

NCs) with RhoB were prepared (Fig. S12.2) and then the release was carried out for both the NCs (Fig. S12.3A-B). For the DTKC-NCs, a ~43% and ~26% release of RhoB were observed for 20% CCM and 20% BM, respectively, after incubation for 25 h. Since the BM does not contain any ROS species and (sub)cellular components, the higher release of 20% CCM can be attributed to these factors (Fig. S12.3A). For the case of pure Dex-NCs, ~29% RhoB release was observed after 30 h, without a significant difference between 20% CCM and 20% BM (Fig. S12.3B) (Wu et al., 2015; Surnar et al., 2015). Since pure dextran nanocarriers have no thioketal linkage, it is safe to presume that the release in CCM is not due to the ROS induced cleavage but rather triggered by other components from CCM and thus did not lead to a difference in release profile between CCM and BM. Comparing both the DTKC and pure dextran NCs, the higher release for the DTKC-NCs under 20% CCM and similar release for both the NCs under 20% BM justifies the ROS induced release in the case of the DTKC-NCs. However, the nanocarriers exhibited greater swelling in 20% BM compared to the control (Milli-Q water), leading to an increased release in 20% BM (Fig. S12.3C, D). The latter could be attributed to the composition of the BM which is different as compared to the control.

Upon exposure of the Dox-loaded NCs to the same release conditions, a total of *ca.* 33.5 ± 1%, 47.1 ± 1.4%, and 70.4 ± 2% cumulative release was observed after 72 h (pH = 7.0) of incubation with 1 mM H_2O_2, 10 mM H_2O_2, and CCM (20% v/v), respectively (Fig. S12.4.1). Recently, a dextran-based micellar system was reported by Guo et al., where Dox was conjugated to dextran using a thioketal linker (Guo et al., 2024) and micelles were prepared with an LC of 8.4%. In this case, Dox release was found to be 65% after incubation with 200 mL of 1 mM H_2O_2 (total 6.8 mg H_2O_2) for 72 h, whereas in our case ~33% release was observed for 16 mL of 1 mM H_2O_2 (total 0.55 mg H_2O_2). In another study by Pan et al., ROS-responsive PEG-DOX conjugate nanoparticles were synthesized and Dox release was found to be 45% after 24 h upon exposure to 30 mL of 0.1 mM H_2O_2 conditions (total 0.11 mg H_2O_2) (Pan et al., 2020). It is worth mentioning that in our case doxorubicin exhibited quenching under the tested conditions (Fig. S12.1) which might be attributed to an underestimation of the values. Regardless, though the nanocarrier systems are different, the results indicate that the release was either slower or comparable to our approach. However, as the drug is encapsulated in our work, chemical conjugation/modification that might influence the efficacy of the drug is averted. Additionally, the approach is generic in incorporating different types of drugs, as demonstrated by the encapsulation of various payloads.

The effect of pH on the release medium was also checked. When incubated with 1 mM and 10 mM H_2O_2 solutions at pH = 5, *ca.* 47% and 62% cumulative release was observed within 26 h of incubation, respectively (Fig. S12.4.2) which is slightly higher than the values observed at pH =7 after the same time. This could be attributed to the combined effect of pH and ROS-responsive release.

Finally, as a proof of concept, the light-triggered release was carried out with the RB loaded NCs. It was hypothesized that irradiation of the NCs would produce $^1O_2$ from the encapsulated RB, which would lead the ROS-responsive NCs to degrade and subsequently cause RB release. When the NCs were irradiated (L(+)) for 10, 20, 30, and 40 minutes, *ca.* 19.7 ± 0.8%, 21.3 ± 0.2%, 17.3 ±0.1%, and 15.2 ± 0.1% release was observed, respectively. The decrement in the release of RB with an increase in light irradiation time could be due to the photobleaching of RB under the measurement conditions (Fig. S12.5). The photobleaching of RB can affect the production of $^1O_2$ by light irradiation and also at the same time reduce the concentration of the remaining RB (unbleached) in the release media. In case of longer irradiation time, the decrease in the concentration of unbleached RB for $^1O_2$ production can eventually lead to the reduction in the cascade reaction with the thioketal bonds and also cause a reduction in the unbleached RB observed in the release media, as observed in the release studies. As a control experiment, the same release was performed with the sample kept in the dark (L(-)), and ~9% release was monitored (Fig. 6B). DLS data indicated a slight D_h and PDI increment upon light irradiation which suggests responsiveness of the NCs to $^1O_2$ (Fig. S12.6). Therefore, we can conclude that light can also act as a trigger to degrade the DTKC-4 NCs in the presence of a photosensitizer for the payload release.

3.6. *In vitro* assessment of the NCs

The biocompatibility of the DTKC-4 NCs was assessed using OSCC cells employing an AlamarBlue cell viability assay. Primarily, the RhoB-NCs incubated OSCC maintained cell viability over 72 h (Fig. 7A). After 24 h specifically, a slight decrease in cell viability was observed when incubated with 50 µg/mL and 100 µg/mL. This decrease can result from cellular adaptation, as cells exposed to environmental changes often undergo an initial period of stress that reduces metabolic activity and therefore the AlamarBlue signal. Moreover, the cell cycle dynamics can play a role in the sensitivity to environmental adaptations; throughout progress, the

cells can restore their metabolic activity whereas they are initially more sensitive (Longhil et al., 2022; Rampersad, 2012). However, cell viability remained above 80%, indicating good biocompatibility of the NCs (López-García, Lehocký, Humpolíček, & Sáha, 2014). Cell viability was also assessed in OSCC cells after incubation with RB-NCs (Fig. S13.1). Similar results for the RhoB-NCs were observed, which shows the biocompatible character of these NCs as well. In addition, the cytotoxic effects of the NCs loaded with Dox were tested for a time period of 72 h. As doxorubicin is cytotoxic, unloaded NCs as well as free Dox were included as a control (Fig. S13.2). Dilution series were prepared for the unloaded NCs analogously to the Dox-loaded NCs (Table S4). The latter showed a declined cell viability over time while unloaded NCs did not reduce cell viability, suggesting the successful *in vitro* release of cargo from the ROS-responsive NCs in OSCC cells. Moreover, previously determined IC50 values for Dox in different OSCC cell lines were up to or equal to concentrations of 1 µg/mL, supporting the obtained doxorubicin cell viability data (Fang et al., 2018). Overall, cell viability results showed that the designed NCs are biocompatible with cancer cells, indicating their potential use in future biomedical applications. In addition, our approach offers an intrinsic advantage in that chemical conjugation of the drug to the carrier is not required. Hence, it offers flexibility in using various therapeutic drugs.

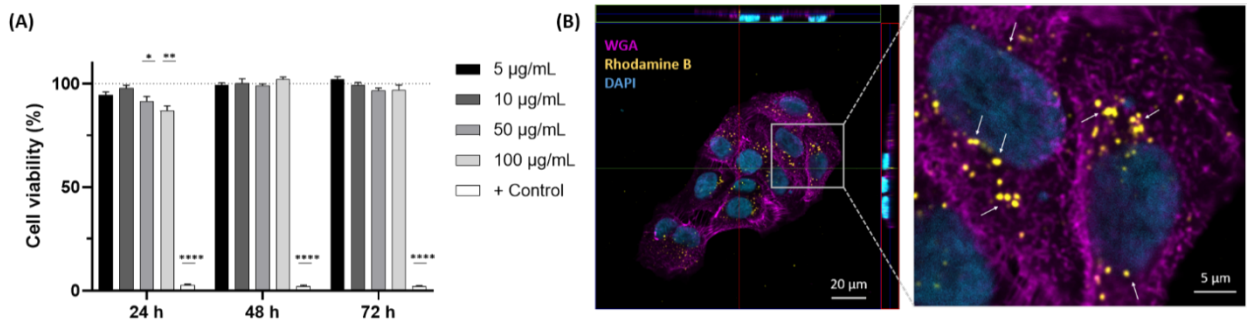

Fig. 7: Cell viability of OSCC cells with the payload (A) RhoB at different concentrations and incubation times (*n=3 biological replicates with 3 technical replicates*) (data are represented as mean±SEM). The dotted line represents the negative control. *P < 0.05, **P < 0.01, and ****P < 0.0001. (B). Confocal image representing cellular uptake of the NCs in the x, y, and z-axis (left) and in higher magnification (right). White arrows indicate NCs. WGA: wheat germ agglutinin; DAPI: 4′,6-diamidino-2-phenylindole.

Subsequently, the uptake of RhoB-NCs by the OSCC cells was investigated. Using flow cytometry, an increased association of the NCs with the cells was detected over time (Fig. S14.1). After 24 h specifically, about 40% of the cells showed a successful association of RhoB-loaded NCs (Fig. S14.2). The obtained confocal microscopy images show that the NCs are successfully

taken up by the cells after incubation with 100 µg/mL for 24 h, more specifically in the perinuclear region (Fig. 7B). Previous studies on the uptake of nanoparticles have demonstrated that exogenous materials entering cells often concentrate in the perinuclear region (Lai, Hida, Chen, & Hanes, 2008; Lai et al., 2007). Collectively, the data indicates that the designed RhoB-NCs are successfully internalized by the cancer cells and do not induce any cytotoxic effects over time.

4. Conclusions

The successful synthesis of water-soluble dextran-thioketal conjugates and further ROS-responsive NCs reported here add to the advancement of polysaccharide-based drug delivery systems. In this systematic study, we showed the versatility of the encapsulation approach, where NCs were capable of encapsulating different water-soluble payloads with a good encapsulation efficiency of > 80%. Interestingly, the EE was also dependent on the cargo type where a high EE >90 % was observed in the case of Doxorubicin. The loading content for the different payloads was between 10-12%, irrespective of their molecular weights and solubility. The nanocarriers were able to release the payloads upon ROS exposure or light irradiation. For the first time, we have demonstrated the light induced cascade reaction to release the encapsulated payload (RB) where $^1O_2$ produced via irradiation of the photosensitizer can subsequently degrade the ROS-responsive NCs. This approach conveniently paves the way for realizing combination therapies, for instance combining a chemotherapeutic drug and a photosensitizer for application in cancer therapy. Further, these nanocarriers showed profound release of hydrophilic payloads irrespective of their payloads in conditioned culture medium, which is the culture medium that was collected after incubation with the OSCC cancer cells, suggesting the applicability of these NCs to release the payloads in a ROS elevated system. The successful uptake and biocompatible character at relevant concentrations of the nanocarriers further validate their potential use in the field of drug delivery to cancer cells. As delivery vehicles for water soluble therapeutic ingredients are highly desired and drug delivery via a stimulus is also highly sought to enable controlled release, this study opens new avenues in exploring dextran-based ROS-responsive NCs for delivering therapeutics employing exogenous as well as endogenous stimuli.

CRediT authorship contribution

Sourav Nayak: Conceptualization, Methodology, Validation, Investigation, Writing - Original Draft, Formal analysis, Visualization. **Nuran Caz:** Investigation, Validation, Formal analysis, Writing-Original draft. **Elien Derveaux**: Methodology, Investigation, Formal analysis. **Sander Smeets**: Investigation and formal analysis, aided by synthesis and characterizations. **Tom Cardeynaels**: Formal analysis and investigation, provided valuable suggestions and discussions. **Esther Wolfs**: Formal analysis, Writing - Review & Editing, Supervision. **Peter Adriaensens**: Methodology, Investigation, Formal analysis, Writing - Review & Editing, Supervision. **Wouter Maes**: Formal analysis, Writing - Review & Editing, Supervision. **Anitha Ethirajan**: Conceptualization, Methodology, Investigation, Formal analysis, Writing - Review & Editing, Supervision, Project administration, Funding acquisition.

Acknowledgments

The authors thank Prof. Karen Smeets (Biodiversity and Toxicology Group, Centre for Environmental Sciences, UHasselt) for providing access to the LSM900 confocal microscope, Birte Luyck for acquiring TEM images, and Dr. Annelies Sels for supporting elemental analysis. Sourav Nayak is funded by the BOF Special Research Fund of Hasselt University (BOF21OWB04). Esther Wolfs and Anitha Ethirajan received funding from the Hasselt University large BOF project program (BOF21GP08). Esther Wolfs is funded by the Research Foundation Flanders (FWO; G040220N and G0A7N24FWO), and Tom Cardeynaels is an FWO postdoctoral fellow (1284623N). The FWO and Hasselt University are acknowledged for the NMR support of this research (AUHL/15/2-GOH3816N).

References

(1) Fatima, M.; Almalki, W. H.; Khan, T.; Sahebkar, A.; Kesharwani, P. Harnessing the Power of Stimuli-Responsive Nanoparticles as an Effective Therapeutic Drug Delivery System. Advanced Materials 2024, n/a (n/a), 2312939. DOI: https://doi.org/10.1002/adma.202312939.

(2) Shi, Y.; Zhang, Y.; Zhu, L.; Miao, Y.; Zhu, Y.; Yue, B. Tailored Drug Delivery Platforms: Stimulus-Responsive Core–Shell Structured Nanocarriers. Advanced Healthcare Materials 2024, 13 (1), 2301726. DOI: https://doi.org/10.1002/adhm.202301726.

(3) Tang, X.; Zhao, S.; Luo, J.; Wang, B.; Wu, X.; Deng, R.; Chang, K.; Chen, M. Smart Stimuli-Responsive Spherical Nucleic Acids: Cutting-Edge Platforms for Biosensing, Bioimaging, and Therapeutics. Small 2024, n/a (n/a), 2310732. DOI: https://doi.org/10.1002/smll.202310732.

(4) Liu, Z.-S.; Wen, J.; Huang, C.-Y.; Zhang, P.-W.; Miao, Y.-L.; Cheng, H.; Li, S.-Y. Nanomedicines Based on Responsive Nanocarriers for Cancer Therapy. Advanced Therapeutics 2024, 7 (2), 2300223. DOI: https://doi.org/10.1002/adtp.202300223.

(5) Mi, P. Stimuli-responsive nanocarriers for drug delivery, tumor imaging, therapy and theranostics. Theranostics 2020, 10 (10), 4557-4588. DOI: https://doi.org/10.7150/thno.38069.

(6) Mura, S.; Nicolas, J.; Couvreur, P. Stimuli-responsive nanocarriers for drug delivery. Nature Materials 2013, 12 (11), 991-1003. DOI: https://doi.org/10.1038/nmat3776.

(7) Zhang, Q.; Kuang, G.; Li, W.; Wang, J.; Ren, H.; Zhao, Y. Stimuli-Responsive Gene Delivery Nanocarriers for Cancer Therapy. Nano-Micro Letters 2023, 15 (1), 44. DOI: https://doi.org/10.1007/s40820-023-01018-4.

(8) Kaushik, N.; Borkar, S. B.; Nandanwar, S. K.; Panda, P. K.; Choi, E. H.; Kaushik, N. K. Nanocarrier cancer therapeutics with functional stimuli-responsive mechanisms. Journal of Nanobiotechnology 2022, 20 (1), 152. DOI: https://doi.org/10.1186/s12951-022-01364-2.

(9) Chang, D.; Ma, Y.; Xu, X.; Xie, J.; Ju, S. Stimuli-Responsive Polymeric Nanoplatforms for Cancer Therapy. Frontiers in Bioengineering and Biotechnology 2021, 9. DOI: https://doi.org/10.3389/fbioe.2021.707319.

(10) Torchilin, V. P. Multifunctional, stimuli-sensitive nanoparticulate systems for drug delivery. Nature Reviews Drug Discovery 2014, 13 (11), 813-827. DOI: https://doi.org/10.1038/nrd4333.

(11) Yang, Y.; Sun, W. Recent advances in redox-responsive nanoparticles for combined cancer therapy. Nanoscale Advances 2022, 4 (17), 3504-3516, 10.1039/D2NA00222A. DOI: https://doi.org/10.1039/D2NA00222A.

(12) Yang, H.; Villani, R. M.; Wang, H.; Simpson, M. J.; Roberts, M. S.; Tang, M.; Liang, X. The role of cellular reactive oxygen species in cancer chemotherapy. Journal of Experimental & Clinical Cancer Research 2018, 37 (1), 266. DOI: https://doi.org/10.1186/s13046-018-0909-x.

(13) Shim, M. S.; Xia, Y. A Reactive Oxygen Species (ROS)-Responsive Polymer for Safe, Efficient, and Targeted Gene Delivery in Cancer Cells. Angewandte Chemie International Edition 2013, 52 (27), 6926-6929. DOI: https://doi.org/10.1002/anie.201209633.

(14) Xu, L.; Zhao, M.; Zhang, H.; Gao, W.; Guo, Z.; Zhang, X.; Zhang, J.; Cao, J.; Pu, Y.; He, B. Cinnamaldehyde-Based Poly(ester-thioacetal) To Generate Reactive Oxygen Species for Fabricating Reactive Oxygen Species-Responsive Nanoparticles. Biomacromolecules 2018, 19 (12), 4658-4667. DOI: https://doi.org/10.1021/acs.biomac.8b01423.

(15) Liu, Y.; Liu, Y.; Zang, J.; Abdullah, A. A. I.; Li, Y.; Dong, H. Design Strategies and Applications of ROS-Responsive Phenylborate Ester-Based Nanomedicine. ACS Biomaterials Science & Engineering 2020, 6 (12), 6510-6527. DOI: https://doi.org/10.1021/acsbiomaterials.0c01190.

(16) Yuan, Y.; Zhang, C.-J.; Liu, B. A Photoactivatable AIE Polymer for Light-Controlled Gene Delivery: Concurrent Endo/Lysosomal Escape and DNA Unpacking. Angewandte Chemie International Edition 2015, 54 (39), 11419-11423. DOI: https://doi.org/10.1002/anie.201503640.

(17) Gao, F.; Xiong, Z. Reactive Oxygen Species Responsive Polymers for Drug Delivery Systems. Frontiers in Chemistry 2021, 9, Review. DOI: https://doi.org/10.3389/fchem.2021.649048.

(18) Tyrrell, Z. L.; Shen, Y.; Radosz, M. Fabrication of micellar nanoparticles for drug delivery through the self-assembly of block copolymers. Progress in Polymer Science 2010, 35 (9), 1128-1143. DOI: https://doi.org/10.1016/j.progpolymsci.2010.06.003.

(19) Arora, S.; Trivedi, R.; Lamptey, R. N. L.; Chaulagain, B.; Layek, B.; Singh, J. 3 - Smart biopolymers for controlled drug delivery applications. In Tailor-Made and Functionalized Biopolymer Systems, Bera, H., Layek, B., Singh, J. Eds.; Woodhead Publishing, 2021; pp 53-83.

(20) Seidi, F.; Jenjob, R.; Phakkeeree, T.; Crespy, D. Saccharides, oligosaccharides, and polysaccharides nanoparticles for biomedical applications. Journal of Controlled Release 2018, 284, 188-212. DOI: https://doi.org/10.1016/j.jconrel.2018.06.026.

(21) Hu, Q.; Lu, Y.; Luo, Y. Recent advances in dextran-based drug delivery systems: From fabrication strategies to applications. Carbohydrate Polymers 2021, 264, 117999. DOI: https://doi.org/10.1016/j.carbpol.2021.117999.

(22) Huang, G.; Huang, H. Application of dextran as nanoscale drug carriers. Nanomedicine 2018, 13 (24), 3149-3158. DOI: https://doi.org/10.2217/nnm-2018-0331.

(23) Pramod, P. S.; Takamura, K.; Chaphekar, S.; Balasubramanian, N.; Jayakannan, M. Dextran Vesicular Carriers for Dual Encapsulation of Hydrophilic and Hydrophobic Molecules and Delivery into Cells. Biomacromolecules 2012, 13 (11), 3627-3640. DOI: https://doi.org/10.1021/bm301583s.

(24) Bao, Y.; Yin, L.; Liu, L.; Chen, L. Acid-sensitive ROS-triggered dextran-based drug delivery system for advanced chemo-photodynamic synergistic therapy. Journal of Biomedical Materials Research Part A 2020, 108 (1), 148-156. DOI: https://doi.org/10.1002/jbm.a.36800.

(25) Alkanawati, M. S.; da Costa Marques, R.; Mailänder, V.; Landfester, K.; Thérien-Aubin, H. Polysaccharide-Based pH-Responsive Nanocapsules Prepared with Bio-Orthogonal Chemistry and Their Use as Responsive Delivery Systems. Biomacromolecules 2020, 21 (7), 2764-2771. DOI: https://doi.org/10.1021/acs.biomac.0c00492.

(26) Fazal, T.; Murtaza, B. N.; Shah, M.; Iqbal, S.; Rehman, M.-u.; Jaber, F.; Dera, A. A.; Awwad, N. S.; Ibrahium, H. A. Recent developments in natural biopolymer based drug delivery systems. RSC Advances 2023, 13 (33), 23087-23121, 10.1039/D3RA03369D. DOI: https://doi.org/10.1039/D3RA03369D.

(27) Perumal, S.; Atchudan, R.; Lee, W. A Review of Polymeric Micelles and Their Applications. Polymers 2022, 14, 2510. DOI: https://doi.org/10.3390/polym14122510.

(28) Rinaldi, A.; Caraffi, R.; Grazioli, M. V.; Oddone, N.; Giardino, L.; Tosi, G.; Vandelli, M. A.; Calzà, L.; Ruozi, B.; Duskey, J. T. Applications of the ROS-Responsive Thioketal Linker for the Production of Smart Nanomedicines. Polymers 2022, 14, 687. DOI: https://doi.org/10.3390/polym14040687.

(29) Tiwari, R., Banerjee, S., Tyde, D., Saha, K. D., Ethirajan, A., Mukherjee, N., Das, A. Redox-Responsive Nanocapsules for the Spatiotemporal Release of Miltefosine in Lysosome: Protection

against Leishmania. Bioconjugate Chemistry 2021, 32(2), 245-253. DOI: https://doi.org/10.1021/acs.bioconjchem.0c00667.

(30) Seneca, S.; Pramanik, S. K.; D'Olieslaeger, L.; Reekmans, G.; Vanderzande, D.; Adriaensens, P.; Ethirajan, A. Nanocapsules with stimuli-responsive moieties for controlled release employing light and enzymatic triggers. Materials Chemistry Frontiers 2020, 4 (7), 2103-2112, 10.1039/D0QM00244E. DOI: https://doi.org/10.1039/D0QM00244E.

(31) Pramanik, S. K.; Pal, U.; Choudhary, P.; Singh, H.; Reiter, R. J.; Ethirajan, A.; Swarnakar, S.; Das, A. Stimuli-Responsive Nanocapsules for the Spatiotemporal Release of Melatonin: Protection against Gastric Inflammation. ACS Applied Bio Materials 2019, 2 (12), 5218-5226. DOI: https://doi.org/10.1021/acsabm.9b00236.

(32) Iyisan, B.; Landfester, K. Modular Approach for the Design of Smart Polymeric Nanocapsules. Macromolecular Rapid Communications 2019, 40 (1), 1800577. DOI: https://doi.org/10.1002/marc.201800577.

(33) Pramanik, S. K., Seneca, S., Peters, M., D'Olieslaeger, L., Reekmans, G., Vanderzande, D., Ethirajan, A. Morphology-dependent pH-responsive release of hydrophilic payloads using biodegradable nanocarriers. RSC Advances 2018, 8(64), 36869-36878. DOI: http://dx.doi.org/10.1039/C8RA07066K.

(34) Yue, C.; Zhang, C.; Alfranca, G.; Yang, Y.; Jiang, X.; Yang, Y.; Pan, F.; Fuente, J. M. d. l.; Cui, D. Near-Infrared Light Triggered ROS-activated Theranostic Platform based on Ce6-CPT-UCNPs for Simultaneous Fluorescence Imaging and Chemo-Photodynamic Combined Therapy. Theranostics 2016, 6 (4), 456-469. DOI: https://doi.org/10.7150/thno.14101.

(35) Kesarwala, A.; Krishna, M.; Mitchell, J. Oxidative stress in oral diseases. Oral Diseases 2016, 22 (1), 9-18. DOI: https://doi.org/10.1111/odi.12300.

(36) Pan, Q.; Deng, X.; Gao, W.; Chang, J.; Pu, Y.; He, B. ROS triggered cleavage of thioketal moiety to dissociate prodrug nanoparticles for chemotherapy. Colloids and Surfaces B: Biointerfaces 2020, 194, 111223. DOI: https://doi.org/10.1016/j.colsurfb.2020.111223.

(37) Guo, Y.; Yang, X.; Zhang, Y.; Luo, F.; Yang, J.; Zhang, X.; Mi, J.; Xie, Y. Hyaluronic acid/dextran-based polymeric micelles co-delivering ursolic acid and doxorubicin to mitochondria for potentiating chemotherapy in MDR cancer. Carbohydrate Polymers 2024, 332, 121897. DOI: https://doi.org/10.1016/j.carbpol.2024.121897.

(38) Singh, D.; Qasam, I.; Paudwal, G.; Kotwal, P.; Behera, C.; Kumar, A.; Gupta, A. P.; Nandi, U.; Yadav, G.; Gupta, P. N.; et al. Redox-Responsive Hyaluronic Acid–Tacrolimus Conjugate: Synthesis, Characterization, and In Vitro Immunosuppressive Activity. ACS Applied Bio Materials 2023, 6 (2), 733-744. DOI: https://doi.org/10.1021/acsabm.2c00946.

(39) Kunc, F.; Moore, C. J.; Sully, R. E.; Hall, A. J.; Gubala, V. Polycarboxylated Dextran as a Multivalent Linker: Synthesis and Target Recognition of the Antibody–Nanoparticle Bioconjugates in PBS and Serum. Langmuir 2019, 35 (14), 4909-4917. DOI: https://doi.org/10.1021/acs.langmuir.8b03833.

(40) Xu, L.; Zhao, M.; Gao, W.; Yang, Y.; Zhang, J.; Pu, Y.; He, B. Polymeric nanoparticles responsive to intracellular ROS for anticancer drug delivery. Colloids and Surfaces B: Biointerfaces 2019, 181, 252-260. DOI: https://doi.org/10.1016/j.colsurfb.2019.05.064.

(41) Lamb, B. M.; Barbas Iii, C. F. Selective arylthiolane deprotection by singlet oxygen: a promising tool for sensors and prodrugs. Chemical Communications 2015, 51 (15), 3196-3199, 10.1039/C4CC09040C. DOI: https://doi.org/10.1039/C4CC09040C.

(42) Moser, M.; Schneider, R.; Behnke, T.; Schneider, T.; Falkenhagen, J.; Resch-Genger, U. Ellman's and Aldrithiol Assay as Versatile and Complementary Tools for the Quantification of Thiol Groups and Ligands on Nanomaterials. Analytical Chemistry 2016, 88 (17), 8624-8631. DOI: https://doi.org/10.1021/acs.analchem.6b01798.

(43) Kuypers, S.; Pramanik, S. K.; D'Olieslaeger, L.; Reekmans, G.; Peters, M.; D'Haen, J.; Vanderzande, D.; Junkers, T.; Adriaensens, P.; Ethirajan, A. Interfacial thiol–isocyanate reactions for functional nanocarriers: a facile route towards tunable morphologies and hydrophilic payload encapsulation. Chemical Communications 2015, 51 (87), 15858-15861, 10.1039/C5CC05258K. DOI: https://doi.org/10.1039/C5CC05258K.

(44) Entradas, T.; Waldron, S.; Volk, M. The detection sensitivity of commonly used singlet oxygen probes in aqueous environments. Journal of Photochemistry and Photobiology B: Biology 2020, 204, 111787. DOI: https://doi.org/10.1016/j.jphotobiol.2020.111787.

(45) Chen, B.; Zhang, Y.; Ran, R.; Wang, B.; Qin, F.; Zhang, T.; Wan, G.; Chen, H.; Wang, Y. Reactive oxygen species-responsive nanoparticles based on a thioketal-containing poly(β-amino ester) for combining photothermal/photodynamic therapy and chemotherapy. Polymer Chemistry 2019, 10 (34), 4746-4757, 10.1039/C9PY00575G. DOI: https://doi.org/10.1039/C9PY00575G.

(46) Lian, H.; Du, Y.; Chen, X.; Duan, L.; Gao, G.; Xiao, C.; Zhuang, X. Core cross-linked poly(ethylene glycol)-graft-Dextran nanoparticles for reduction and pH dual responsive intracellular drug delivery. Journal of Colloid and Interface Science 2017, 496, 201-210. DOI: https://doi.org/10.1016/j.jcis.2017.02.032.

(47) Zeini, D.; Glover, J. C.; Knudsen, K. D.; Nyström, B. Influence of Lysine and TRITC Conjugation on the Size and Structure of Dextran Nanoconjugates with Potential for Biomolecule Delivery to Neurons. ACS Applied Bio Materials 2021, 4 (9), 6832-6842. DOI: https://doi.org/10.1021/acsabm.1c00544.

(48) Su, C.-M.; Lin, C.; Huang, C.-Y.; Yeh, J.-C.; Tsai, T.-Y.; Ger, T. R.; Wang, M.-C.; Lou, S.-L. Dextran-g-lauric acid as IKK complex inhibitor carrier. RSC Advances 2017, 7 (89), 56247-56255, 10.1039/C7RA04544A. DOI: https://doi.org/10.1039/C7RA04544A.

(49) Nikonenko, N. A., Buslov, D. K., Sushko, N. I., & Zhbankov, R. G. Investigation of stretching vibrations of glycosidic linkages in disaccharides and polysaccarides with use of IR spectra deconvolution. Biopolymers 2000, 57(4), 257-262. DOI: https://doi.org/10.1002/1097-0282(2000)57:4<257::AID-BIP7>3.0.CO;2-3.

(50) Liu, B.; Thayumanavan, S. Mechanistic Investigation on Oxidative Degradation of ROS-Responsive Thioacetal/Thioketal Moieties and Their Implications. Cell Reports Physical Science 2020, 1 (12), 100271. DOI: https://doi.org/10.1016/j.xcrp.2020.100271.

(51) Rudyk, O.; Eaton, P. Biochemical methods for monitoring protein thiol redox states in biological systems. Redox Biology 2014, 2, 803-813. DOI: https://doi.org/10.1016/j.redox.2014.06.005.

(52) Cathell, M. D.; Szewczyk, J. C.; Bui, F. A.; Weber, C. A.; Wolever, J. D.; Kang, J.; Schauer, C. L. Structurally Colored Thiol Chitosan Thin Films as a Platform for Aqueous Heavy Metal Ion Detection. Biomacromolecules 2008, 9 (1), 289-295. DOI: https://doi.org/10.1021/bm700845z.

(53) Kukreja, R. C.; Kearns, A. A.; Zweier, J. L.; Kuppusamy, P.; Hess, M. L. Singlet oxygen interaction with Ca(2+)-ATPase of cardiac sarcoplasmic reticulum. Circulation Research 1991, 69 (4), 1003-1014. DOI: https://doi.org/10.1161/01.RES.69.4.1003.

(54) Winther, J. R., & Thorpe, C.; Quantification of thiols and disulfides. Biochimica et Biophysica Acta (BBA) - General Subjects 2014, 1840(2), 838-846. DOI: https://doi.org/10.1016/j.bbagen.2013.03.031.

(55) van Bergen, L. A. H.; Roos, G.; De Proft, F. From Thiol to Sulfonic Acid: Modeling the Oxidation Pathway of Protein Thiols by Hydrogen Peroxide. The Journal of Physical Chemistry A 2014, 118 (31), 6078-6084. DOI: https://doi.org/10.1021/jp5018339.

(56) Nayak, S.; Vanheusden, C.; Leendertse, T.; Schruers, L.; Luyck, B.; Merchiers, J.; D'Haen, J.; Buntinx, M.; Reddy, N.; Ethirajan, A. Centrifugally spun hybrid polyhydroxyalkanoate/dextran nanocapsule fiber matrix for the delivery of hydrophilic payloads. Colloids and Surfaces A: Physicochemical and Engineering Aspects 2023, 675, 132043. DOI: https://doi.org/10.1016/j.colsurfa.2023.132043.

(57) Ding, C.; Shi, Z.; Ou, M.; Li, Y.; Huang, L.; Wang, W.; Huang, Q.; Li, M.; Chen, C.; Zeng, X.; et al. Dextran-based micelles for combinational chemo-photodynamic therapy of tumors via in vivo chemiluminescence. Carbohydrate Polymers 2023, 319, 121192. DOI: https://doi.org/10.1016/j.carbpol.2023.121192.

(58) Sun, C.; Liang, Y.; Hao, N.; Xu, L.; Cheng, F.; Su, T.; Cao, J.; Gao, W.; Pu, Y.; He, B. A ROS-responsive polymeric micelle with a π-conjugated thioketal moiety for enhanced drug loading and efficient drug delivery. Organic & Biomolecular Chemistry 2017, 15 (43), 9176-9185, 10.1039/C7OB01975K. DOI: https://doi.org/10.1039/C7OB01975K.

(59) Malzahn, K., Marsico, F., Koynov, K., Landfester, K., Weiss, C. K., & Wurm, F. R. Selective Interfacial Olefin Cross Metathesis for the Preparation of Hollow Nanocapsules. ACS Macro Letters 2014, 3(1), 40-43. DOI: https://doi.org/10.1021/mz400578e.

(60) Schlegel, I., Renz, P., Simon, J., Lieberwirth, I., Pektor, S., Bausbacher, N., Landfester, K. Highly Loaded Semipermeable Nanocapsules for Magnetic Resonance Imaging. Macromolecular Bioscience 2018, 18(4), 1700387. DOI: https://doi.org/10.1002/mabi.201700387.

(61) Bacher, L., Maskos, M., & Musyanovych, A. Gelatin-Based Capsules through Interfacial Polymerization: Batch and Continuous Flow Synthesis. Chemical Engineering & Technology 2019, 42(10), 2119-2126. DOI: https://doi.org/10.1002/ceat.201900119.

(62) Jagielski, N.; Sharma, S.; Hombach, V.; Mailänder, V.; Rasche, V.; Landfester, K. Nanocapsules Synthesized by Miniemulsion Technique for Application as New Contrast Agent

Materials. Macromolecular Chemistry and Physics 2007, 208 (19-20), 2229-2241. DOI: https://doi.org/10.1002/macp.200700254.

(63) Zhang, W.; Hu, X.; Shen, Q.; Xing, D. Mitochondria-specific drug release and reactive oxygen species burst induced by polyprodrug nanoreactors can enhance chemotherapy. Nature Communications 2019, 10 (1), 1704. DOI: https://doi.org/10.1038/s41467-019-09566-3.

(64) Wang, Z.; Ju, Y.; Ali, Z.; Yin, H.; Sheng, F.; Lin, J.; Wang, B.; Hou, Y. Near-infrared light and tumor microenvironment dual responsive size-switchable nanocapsules for multimodal tumor theranostics. Nature Communications 2019, 10 (1), 4418. DOI: https://doi.org/10.1038/s41467-019-12142-4.

(65) Xu, L.; Zhao, M.; Yang, Y.; Liang, Y.; Sun, C.; Gao, W.; Li, S.; He, B.; Pu, Y. A reactive oxygen species (ROS)-responsive low molecular weight gel co-loaded with doxorubicin and Zn(ii) phthalocyanine tetrasulfonic acid for combined chemo-photodynamic therapy. Journal of Materials Chemistry B 2017, 5 (46), 9157-9164, 10.1039/C7TB02359F. DOI: https://doi.org/10.1039/C7TB02359F.

(66) Wu, Y.-W.; Huang, C.-C.; Changou, C. A.; Lu, L.-S.; Goubran, H.; Burnouf, T. Clinical-grade cryopreserved doxorubicin-loaded platelets: role of cancer cells and platelet extracellular vesicles activation loop. Journal of Biomedical Science 2020, 27 (1), 45. DOI: https://doi.org/10.1186/s12929-020-00633-2.

(67) Wu, Y.; Chu, Q.; Tan, S.; Zhuang, X.; Bao, Y.; Wu, T.; Zhang, Z. D-α-tocopherol polyethylene glycol succinate-based derivative nanoparticles as a novel carrier for paclitaxel delivery. Int J Nanomedicine 2015, 10, 5219-5235. DOI: https://doi.org/10.2147/ijn.S82847.

(68) Surnar, B.; Sharma, K.; Jayakannan, M. Core–shell polymer nanoparticles for prevention of GSH drug detoxification and cisplatin delivery to breast cancer cells. Nanoscale 2015, 7 (42), 17964-17979, 10.1039/C5NR04963F. DOI: https://doi.org/10.1039/C5NR04963F.

(69) Longhin, E. M.; El Yamani, N.; Rundén-Pran, E.; Dusinska, M. The alamar blue assay in the context of safety testing of nanomaterials. Frontiers in Toxicology 2022, *4*, Methods. DOI: https://doi.org/10.3389/ftox.2022.981701.

(70) Rampersad, S. N. Multiple Applications of Alamar Blue as an Indicator of Metabolic Function and Cellular Health in Cell Viability Bioassays. Sensors 2012, *12* (9), 12347-12360. DOI: https://doi.org/10.3390/s120912347.

(71) López-García, J.; Lehocký, M.; Humpolíček, P.; Sáha, P. HaCaT Keratinocytes Response on Antimicrobial Atelocollagen Substrates: Extent of Cytotoxicity, Cell Viability and Proliferation. In Journal of Functional Biomaterials 2014, 5, 43-57. DOI: https://doi.org/10.3390/jfb5020043.

(72) Fang, L.; Gao, L.; Xie, L.; Xiao, G. Eukaryotic translation initiation factor 5A-2 involves in doxorubicin-induced epithelial-mesenchymal transition in oral squamous cell carcinoma cells. Journal of Cancer 2018, *9* (19), 3479-3488. DOI: https://doi.org/10.7150/jca.26136.

(73) Lai, S. K.; Hida, K.; Chen, C.; Hanes, J. Characterization of the intracellular dynamics of a non-degradative pathway accessed by polymer nanoparticles. Journal of Controlled Release 2008, 125 (2), 107-111. DOI: https://doi.org/10.1016/j.jconrel.2007.10.015.

(74) Lai, S. K.; Hida, K.; Man, S. T.; Chen, C.; Machamer, C.; Schroer, T. A.; Hanes, J. Privileged delivery of polymer nanoparticles to the perinuclear region of live cells via a non-clathrin, non-degradative pathway. Biomaterials 2007, 28 (18), 2876-2884. DOI: https://doi.org/10.1016/j.biomaterials.2007.02.021.